Buss, H. L., Brantley, S. L., Scatena, F. N., Bazilievskaya, E. A., Blum, A., Schulz, M., Jimenez, R., White, A. F., Rother, G., & Cole, D. (2013). Probing the deep critical zone beneath the Luquillo Experimental Forest, Puerto Rico. *Earth Surface Processes and Landforms*, *38*(10), 1170-1186. https://doi.org/10.1002/esp.3409

Probing the deep critical zone beneath the Luquillo Experimental Forest, Puerto Rico

Journal:	*Earth Surface Processes and Landforms*
Manuscript ID:	ESP-12-0050.R1
Wiley - Manuscript type:	Special Issue Paper
Date Submitted by the Author:	n/a
Complete List of Authors:	Buss, Heather; University of Bristol, Earth Sciences Brantley, Susan; Penn State University, Earth & Environmental Systems Institute Scatena, Frederick; University of Pennsylvania, Earth and Environmental Science Bazilevskaya, Ekaterina; Penn State University, Earth & Environmental Systems Institute Blum, Alex; US Geological Survey, Water Resources Schulz, Marjorie; US Geological Survey, Water Resources Jiménez, Rafael; University of Pennsylvania, Earth and Environmental Science White, Art; USGS, Water Resources Rother, Gernot; Oak Ridge National Laboratory, Chemical Sciences Division Cole, David; Ohio State University, School of Earth Sciences
Keywords:	critical zone, weathering, drilling, corestones, regolith

Revised submission for the special issue of ESPL on deep CZ

Probing the deep critical zone beneath the Luquillo Experimental Forest, Puerto Rico

[1,*]Buss H.L., [2]Brantley S.L., [3]Scatena F.N., [2]Bazilievskaya E.A., [4]Blum A., [5]Schulz M., [3]Jiménez R., [5]White A.F., [6]Rother G., [7]Cole D.

[1]School of Earth Sciences, University of Bristol, Wills Memorial Building, Bristol BS8 1RJ, UK
[2]Earth and Environmental Systems Institute, The Pennsylvania State University, University Park, PA, 16802, USA
[3]Department of Earth and Environmental Sciences, University of Pennsylvania, 230 S 33rd Street, Philadelphia, PA 19104, USA
[4]U.S. Geological Survey, 3215 Marine Street, Boulder, CO 80303, USA
[5]U.S. Geological Survey, 345 Middlefield Road, MS 420, Menlo Park, CA 94025, USA
[6]Chemical Sciences Division, Oak Ridge National Laboratory, Oak Ridge, TN 37831, USA
[7]School of Earth Sciences, Ohio State University, Columbus, OH 43210 USA

*Corresponding author: h.buss@bristol.ac.uk

20 January 2013

Short Title: Luquillo deep critical zone

Keywords: Critical zone, drilling, corestones, regolith, weathering

Abstract

Recent work has suggested that weathering processes occurring in the subsurface produce the majority of silicate weathering products discharged to the world's oceans, thereby exerting a primary control on global temperature via the well-known positive feedback between silicate weathering and CO_2. In addition, chemical and physical weathering processes deep within the *critical zone* create aquifers and control groundwater chemistry, watershed geometry and regolith formation rates. Despite this, most weathering studies are restricted to the shallow critical zone (e.g., soils, outcrops). Here we investigate the chemical weathering, fracturing and geomorphology of the deep critical zone in the Bisley watershed in the Luquillo Critical Zone Observatory, Puerto Rico, from two boreholes drilled to 37.2 and 27.0 m depth, from which continuous core samples were taken. Corestones exposed aboveground were also sampled. Weathered rinds developed on exposed corestones and along fracture surfaces on subsurface rocks slough off of exposed corestones once rinds attain a thickness up to ~1 cm, preventing the corestones from rounding due to diffusion limitation. Such corestones at the land surface are assumed to be what remains after exhumation of similar, fractured bedrock pieces that were observed in the drilled cores between thick layers of regolith. Some of these subsurface corestones are massive and others are highly fractured, whereas aboveground corestones are generally massive with little to no apparent fracturing. Subsurface corestones are larger and less fractured in the borehole drilled on a road where it crosses a ridge compared to the borehole drilled where the road crosses the stream channel. Both borehole profiles indicate that the weathering zone extends to well below the stream channel in this upland catchment; hence weathering depth is

not controlled by the stream level within the catchment and not all of the water in the watershed is discharged to the stream.

Introduction

Weathering of bedrock is the initial step in the soil-forming process and the primary contributor of solutes and sediments to the hydrosphere. However, the interfaces where intact bedrock weathers to disaggregated material (e.g., corestones and saprolite) are often hidden deep within the critical zone. The vast majority of weathering studies in the natural environment focus on the shallow critical zone: soils, sediments, regolith, saprolite, and outcrops within several meters of the land surface. Although weathering processes have been quantified in these surficial zones, it is likely that weathering of primary minerals along bedrock fractures located in the groundwater or deeper vadose zones supplies significant weathering products to streams and oceans (Anderson and Dietrich, 2001; Calmels et al., 2011; Kurtz et al., 2011; Tipper et al., 2006a; Tipper et al., 2006b). These observations may be particularly important in the tropics, where weathering forms saprolites tens or even hundreds of meters thick (Ollier and Pain, 1996). Weathered materials from such depths are extremely difficult to retrieve and are thus rarely studied.

Many models of weathering and landscape evolution rely on assumptions of steady state regolith thickness wherein the rates of bedrock weathering and physical erosion are assumed to be equal. Only a few studies have tested this assumption by comparing erosion rates measured by cosmogenic isotopes to regolith production rates measured by U-Th disequilibria (e.g., Dosseto et al., 2012; Dosseto et al., 2008). Furthermore, only a few researchers have proposed feedbacks that might

control such coupling (e.g., Fletcher et al., 2006; Riebe et al., 2004; West et al., 2005). A further complication is that some researchers consider such steady-state assumptions to only be applicable to the "mobile soil" that moves down hillslopes (Dietrich et al., 1995; Heimsath et al., 1997) while others assume steady state for the entire soil + saprolite + incipiently weathered rock zone (e.g., Fletcher et al., 2006; White, 2002). In the former case, erosion and weathering advance might be coupled only over a few tens of centimeters while in the latter case the two processes might be coupled to tens of meters. A few researchers have suggested that biota may act to couple surface erosion to the production of weathered material in the "mobile soil" layer (e.g., Roering et al., 2010). Alternatively, Fletcher and others suggested that pore water chemistry and weathering particle size distributions might couple surficial erosion to weathering advance even to hundreds of meters depth (Brantley et al., 2011; Fletcher and Brantley, 2010; Fletcher et al., 2006). Nonetheless, no fully coupled model has been proposed for either shallow "mobile soil" or deeper regolith systems.

In contrast, an apparent *de*coupling of deep and surficial nutrient cycles has been noted in the tropics and subtropics due to isolation of ecosystems by highly weathered, deep (~10's to 100's of m) regoliths of, which are typically depleted in base cations and mineral nutrients such as Ca, Mg, and P (e.g., Bruijnzeel, 1991). For example, in the Luquillo Critical Zone Observatory (LCZO) in northeastern Puerto Rico (Figure 1), thick regolith blankets the landscape. At ridge tops, where hydrologic flow from the surface to the deep regolith is effectively 1-D, this thick, nutrient-poor regolith effectively isolates microbial communities at depth from the ecosystems at the surface, as evidenced by depth profiles of solid and solute organic

carbon, mineral nutrients, and microbial cell densities (e.g., Murphy, 1995; White et al., 1998; Buss et al., 2005; Buss et al., 2010a,b).

In addition to ecological decoupling, chemical weathering in the humid tropics may also be decoupled by thick, highly leached regolith, such that chemical export budgets are dominated by weathering along fractures in the subsurface. Therefore, the density, spacing, connectivity, and transmissivity of bedrock fractures and the groundwater residence time may exert significant control on chemical weathering fluxes out of watersheds. In the granitic Rio Icacos watershed of the LCZO, Si/Ge ratios and Si isotopes indicate that mineral weathering reactions that occur only at the bedrock-saprolite interface (plagioclase and amphibole dissolution) are the dominant source of the dissolved Si to the river during baseflow (Kurtz et al., 2011; Lugolobi et al., 2010; Ziegler et al., 2005). Kurtz et al. (2011) also showed that the rising limbs of storm hydrographs in the Rio Icacos were dominated by groundwater, coinciding with a pulse of solutes from fracture-sourced weathering reactions. As the storms progressed, the hydrologic flux became dominated by more dilute water sources: rainwater and surficial runoff, finally returning to groundwater-dominated flow as the hydrograph returned to baseflow conditions after several hours.

Given the expense and difficulty of sampling deep (10's to 100's of m; i.e, below the hand-augerable regolith) into the critical zone, it is common that investigators make extrapolations or inferences about weathering processes at depth. It is rare that drilling can accompany a weathering study to test these inferences. Furthermore, well drilling typically does not include continuous core sampling, especially within highly fractured and partially weathered rock, which is technically difficult to accomplish. In this contribution, we report the first results of drilling in one of the watersheds under study within the LCZO: Bisley. In that

watershed, one of the notable weathering features are angular boulders that have been exposed at the land surface (Fletcher and Brantley, 2010; Pike et al., 2010). Both of those studies noted that, on average, the size of the largest of these boulders at any location decreases upward as elevation increases (see schematic shown in Figure 2). Although some boulders may have been transported, this is not expected to have altered the general relationship between the size of the largest boulders and elevation. Fletcher and Brantley mapped these boulders throughout the Bisley watershed whereas Pike et al. measured sediment sizes in the river beds. Based on these boulders, a series of hypotheses were made about the subsurface and we test those hypotheses here.

Specifically, Fletcher and Brantley (2010) proposed that the changing size of boulders is due to a previous regime of weathering (Stage 1 in Figure 2) that is now being incised by the Bisley stream (Stage 2, Fig. 2, also see Figure 3). A longitudinal profile of the Bisley I channel is shown in Figure 3 (Fletcher and Brantley, 2010), which extends from the headwaters, past the Bisley I outlet (260 masl), and continues along the main stem of the Bisley tributary (Bisley tributaries I and II join the larger Bisley III). Just above 50 masl, the combined Bisley tributary joins the main stem of the Rio Mameyes, where the river is bedrock-lined. Within the Bisley I watershed, the size of the boulders at the land surface decreases upward with elevation *only above ~200 masl* (below 200 masl, boulder size was invariant). Fletcher and Brantley inferred that these boulders were formed in the subsurface as water infiltrated into fractured rock; after weathering, the rocks became smaller with time to form angular “corestones.” By fitting a model for corestone development during weathering to the size-elevation data, they inferred that the range in elevation over which corestones vary in size – ~200 m – corresponds to a ~135 meter-thick

weathering layer that today contains angular boulders surrounded by saprolite. Beneath this 135 meter-thick layer, they hypothesized that bedrock was still fractured but insignificantly weathered– they termed this the weathering, or corestone, baseline. Corestones of roughly the same size (due to equal fracture spacing) were assumed to emerge from this baseline at 135 m depth. As corestones interacted with infiltrating fluids, they became smaller with time. The model is consistent with a depth to the corestone baseline of ~100 m at the uppermost ridge of the Bisley I catchment and ~30 m at the outlet of Bisley I. The gradient of the corestone baseline was inferred to be identical to the Bisley stream above its confluence with the Mameyes. Thus, the Bisley stream was assumed to be eroding into an already weathered layer of saprolite+corestones. While the authors argued that the deep weathering had been previously imposed on the system, they pointed out that it is also possible that the deep weathering is ongoing today such that weathering and erosion are coupled to depths possibly exceeding 100 m.

The model just summarized is not well constrained by data other than observations of corestone size at land surface. Nonetheless, other researchers have made similar estimates of depth to un-weathered bedrock (Schellekens et al., 2004). Here, we report results from drilling at the mouth of the Bisley I catchment (260 masl) where we tried to drill to the un-weathered bedrock to gain insight into how subsurface CZ processes influence the structure, character, and properties of the more readily observable, surficial CZ. We hypothesized that the corestone-containing zone would terminate in fractured bedrock at about 30 m depth (230 masl), based on Fig. 3 in Fletcher and Brantley (2010) and Fig. 4 in Schellekens et al. (2004). Furthermore, since smaller corestones exposed at the land surface at higher elevations are presumed to have weathered for longer than larger corestones

at lower elevations, we also hypothesized that weathering rinds on large and small corestones (at low and high elevations, respectively) would differ. To investigate that inference, we also present chemical evidence identifying the weathering reactions within the saprolite and within the weathering rinds on the angular corestones.

Field Setting

The Luquillo Mountains in northeastern Puerto Rico are characterized by steep, rugged slopes, highly dissected valleys, a hot and humid climate, and dense, tropical vegetation that grows over deep, highly weathered saprolites. The Luquillo Mountains host the 113-km^2 Luquillo Experimental Forest (LEF), a research preserve administered by the U.S. Forest Service that has been designated a critical zone observatory (CZO) by the National Science Foundation. Several large river systems drain the LEF north to the Atlantic Ocean (Rio Mameyes, Rio Sabana, Rio Espiritu Santo, and Rio Fajardo) or south to the Caribbean Sea (Rio Blanco).

The Bisley experimental watersheds are a sequence of adjacent catchments (numbered 1-5, from east to west) that drain into the Rio Mameyes (Figure 1). Elevation in the 44 km² (17.8 km^2 gaged area) Rio Mameyes watershed ranges from 80 to 1050 masl. The Bisley watersheds are covered by mature Tabonuco type forest and have elevation that ranges from 260-400 masl and drainages from 6-50 ha in area (Scatena, 1989). The climate is humid, subtropical and has precipitation in every month. Mean monthly temperatures average about 24° C in the winter and about 27.5° C in the summer (Schellekens et al., 2004); National Weather Service, 2007). Rainfall increases with altitude in the Luquillo Mountains, from about 2,500 to 4,500 mm y^{-1} over 1,200 m of elevation (Garcia-Martino et al., 1996). The Bisley

watersheds experienced an average rainfall of 3482 mm y^{-1} between 1988 and 2003 (Heartsill-Scalley et al., 2007). Surface hydrology is characterized by intense rainfall and rapid streamflow response that is dominated by fast, near-surface flow paths (Schellekens et al., 2004).

The Bisley watersheds are underlain by bedrock of the ~100 Ma, basaltic to andesitic, marine-bedded, volcaniclastic Fajardo formation (Jolly et al., 1998). This formation developed from a near-sea level volcanic complex that produced pyroclastic debris that was deposited in a shallow marine environment after transport and re-working (Seiders, 1971). The Fajardo formation likely underwent weak contact metamorphism during the intrusion of the nearby Rio Blanco quartz diorite stock 49-42 Ma (Smith et al., 1998). The Bisley catchments are underlain by an upper thick-bedded tuff unit of the Fajardo formation which includes some breccias, lithic andesitic clasts, calcareous siltstone, and some pumice and red scoria (Briggs and Cortes-Aguilar, 1980).

Ridges in the Bisley watersheds are mantled by thick (> 9 m), highly cohesive regolith (including soil, saprolite, and/or transported material). Ridgetop soils are Ultisols of the Humatas Series, which are 0.8-1.0 m deep, moderately well-drained, very-fine, parasesquic, isohyperthermic Typic Haplohumults (Scatena, 1989; Silver et al., 1994; USDA NCRS, 2002). Hand-augered regolith cores to 9 m depth in the valley and 16 m depth on the highest ridge revealed highly weathered saprolite nearly devoid of primary minerals (Dosseto et al., 2012; Frizano et al., 2002).

Landslides, soil creep, and tree throws incise and sharpen the ridges, and leave high-angle hillslopes with thinner regolith (typically 1 to 3 m deep). Most slopes, lower-elevation ridges, and valleys are riddled with exposed corestones. Stream gradients in and around the Bisley catchments are steep, and hillslopes are

generally convex-concave in form. Specifically, the upper slope segments are convex-upward, whereas middle sections are typically straight. The lower slope segments are usually concave-upward when they pass into first order valleys and straight where they join the main channel. More than half of the catchment has slopes greater than 45% (Scatena, 1989). On an aerial basis, the Bisley landscape is comprised of 17% ridges, 18% valleys and 65% slopes (Scatena and Lugo, 1995). Shallow earth movement, soil creep and tree fall are important geomorphic processes and previous research has indicated strong interrelationships between topographic position, landscape stability, and soil and forest development (Heartsill-Scalley et al., 2010; Scatena and Lugo, 1995; Silver et al., 1994). In general, ridges are the most stable landforms, have the oldest stands of vegetation, highest biomass, and the most soil organic matter and acid-leached soils (Scatena and Lugo, 1995).

To investigate the geometry of the Bisley subsurface, Schellekens et al. (2004) used hand augering and geo-electric sounding along the Bisley II stream channel (~150 m southwest of the Bisley I stream channel) and along the ridge that divides the Bisley I and II catchments. Their results were interpreted to show a deep and spatially continuous bedrock-saprolite interface that runs parallel to the elevation-profile of the stream channel, but is not parallel to the overall surface topography(Schellekens et al., 2004).

Methods

Drilling and sample collection

Exposures of in-place bedrock (as opposed to corestones) are rare in the Bisley watersheds due to dense vegetation and thick regolith. Boulders, interpreted as corestones either in place or transported only short distances, were sampled from locations at 234 to 369 m elevation along the Bisley I stream bank using a hand-held, gas powered paleomagnetic drill equipped with a diamond-encrusted coring drill bit 2 cm in diameter. Cores varied from 2 to 20 cm in length. In every case, angular corestones were exposed at the land surface and the cores were collected approximately perpendicular to the exposed corestone surface. The size of the corestone was also estimated. Each corestone was roughly measured in 3 dimensions with a measuring tape to ± 0.5 m and corestone size was estimated as the cube root of the product of the 3 dimensions following our earlier methodology (Fletcher and Brantley, 2010). Corestone sampling locations and descriptions are given in Table 1. Several corestones exposed by landslides were also sampled using a rock hammer (Tables 2-3).

In addition to the core-drilling of the exposed boulders, we also investigated deep, un-exposed bedrock from two 9.6 cm diameter (HQ) boreholes drilled to 37.2 and 27.0 m depth (B1W1 and B1W2, respectively) along Road 915 (B1W1: N18 18.933 W65 44.748, B1W2: N18 18,958 W65 44.726, referenced to the NAD83 datum; Figure 1), near the Bisley I stream gage. Drilling was done by Geo Cim Inc. (Guaynabo, Puerto Rico) with a hydraulic rotary drill with diamond-impregnated drill bits, using only water from the Bisley I stream as drilling fluid. Continuous core samples through coherent rock were taken during drilling using an HQ-wireline barrel.

Analyses

Bulk solid-state chemical analysis was performed on pulverized and sieved (150 μm) rock and saprock samples. Solid samples were digested by lithium metaborate fusion and major and minor elements were determined by inductively coupled plasma atomic emission spectrometry (ICP-AES) at the SGS Mineral Laboratories, Ontario, Canada. Additional solid samples underwent a multi-acid digest and analysis for ferrous iron by wet chemical methods (SGS Mineral Laboratories, Ontario, Canada). The Chemical Index of Alteration (CIA) was calculated from the bulk elemental chemistry (Nesbitt and Young, 1982):

$$CIA = 100 \frac{Al_2O_3}{Al_2O_3 + CaO + Na_2O + K_2O} \quad (1).$$

The CIA documents the loss of mobile base cations Ca, Na, and K relative to Al, which is assumed to be relatively immobile. Values of the CIA increase with increasing degree of weathering to a maximum of 100. Fresh rock is typically ≤ 50.

Powder X-ray diffraction was performed at the USGS (Boulder, CO), using a Siemens D500 diffractometer. Quantitative mineral abundances were determined from powder X-ray diffraction data using the computer program ROCKJOCK (Eberl, 2003) and compared to bulk chemical abundances using HandLens (Eberl, 2008). Thin sections were prepared from rock, weathered rock fragments, and saprock samples (Spectrum Petrographics, Vancouver, WA, USA). Thin sections were examined using an optical petrographic microscope and a field-emission scanning electron microscope (model Leo-982; Carl Zeiss SMT Inc., Peabody, MA) equipped with an energy dispersive spectroscopy (EDS) detector. Samples were prepared for SEM by vacuum coating with Au.

Hand-drilled core samples of corestones collected along the Bisley I stream (Table 1) were cut lengthwise, perpendicular to the rind-rock interface, to prepare 0.15 mm thick petrographic thin sections (Tulsa Section Incorporated, Coweta, Oklahoma, USA). Mineral composition and morphology were examined using an optical petrographic microscope and a Hitachi SEM unit (model S-3500N) coupled with a Princeton Garmon Tech EDS unit at the Materials Characterization Laboratory (MCL), Penn State. The spatial chemical variability across the rock-rind boundary were studied by measuring Si, Ca, Al, Ti, Fe, Na, and Mg along a ~10 mm transect on four 2 mm thick sections across the rock–rind boundary. In addition, the thicknesses of the weathering rinds were estimated using image-processing software (ImageJ). Bulk chemical compositions were measured on the corestone samples by carefully separating un-weathered rock from weathered rinds and analyzing them separately ICP-AES, at MCL, Penn State.

Mass transfer coefficients, $\tau_{i,j}$, were calculated from the elemental transect data collected on the corestone thin sections. “Tau” ratios concentrations of mobile elements to concentrations of a relatively immobile element (here Al) to document the mass transfer (loss or gain) of an element *j* relative to the parent rock composition (Anderson et al., 2002; Brimhall and Dietrich, 1987). Here the deepest analysis of each transect was used as the parent composition.

$$\tau_{Al,j} = \left(\frac{C_{j,w} C_{Al,p}}{C_{j,p} C_{Al,w}} \right) - 1 \qquad (2).$$

Here, $C_{j,w}$ is the mass fraction of element *j* in the weathered material, and $C_{j,p}$ is the mass fraction of element *j* in the parent material. If $\tau_{Ti,j}$ = -1, element *j* is entirely lost. If $\tau_{Ti,j}$ > 0, a net gain of element *j* relative to the parent rock is indicated.

Two corestones exposed at different elevations were sampled for neutron scattering (NS) analysis: DR-4 and DR-7 (Table 5). Both samples consist of fine-grained slightly metamorphosed volcaniclastic siltstone. These samples were chosen for their similar texture (fine-grained) and rind thickness. Double-polished thick sections were prepared from samples cut perpendicular to the core-rind interface following methods in the literature (Jin et al., 2011). Under optical microscopy, the cores of both samples were grey in color. In DR-7, the grey core grades into a tan-colored zone followed by zones of white, then red. In DR-4, the grey core grades into a brownish zone followed by zones of pink, then red. Under optical microscopy, grain size within the rind of DR-4 is visibly larger and more variable than in the rind of DR-7.

Small-angle neutron scattering (SANS) measurements were conducted on beamline NG7 at the National Center for Neutron Research (NCNR) of the National Institute of Standard and Technology (NIST, Gaithersburg, USA). Using a wave length (λ) for neutrons of 8.09 Å, the scattered intensity was measured at sample to detector distances of 1.0, 4.0, and 15.0 m using a 2D detector for neutrons with different values of the scattering vector (Q). Thin sections were mounted behind a cadmium plate with a 1 mm x 15.9 mm slit used to mask most of the incident neutron beam. Neutrons were only allowed to pass through the slit, which was positioned parallel to the line defining the visually observable rind-core interface. The 1 mm-thick Cd mask was moved sequentially to scatter neutrons from areas of dimension 1 mm x 15.9 mm moving from the edge of the rind to the fresh rock (Fig. 6A, F). However, because an orientation notch was cut into each section, the actual illuminated sample area was reduced in the rind with respect to the fresh rock part in which no notch was present. The varying illuminated areas were measured and

appropriate scaling factors applied ot normalize scattering intensities to the respective sample volumes. The SANS data were corrected for neutron transmission, empty quartz wafer scattering and blocked beam (dark current). Normalization to the empty beam current was used for absolute scattering intensity calibration (Kline, 2006).

Ultra-small angle neutron scattering (USANS) data were obtained on the BT5 beamline at NCNR NIST, Gaithersburg, USA for the same set of samples in a similar fashion. The USANS data were corrected for empty cell scattering and transmission and de-smeared using the NIST data reduction routines (Kline, 2006). Finally, the corrected and normalized SANS and USANS data sets were combined into one scattering curve as described in Jin et al. (2011).

In SANS and USANS, the scattered intensity, I(Q), is measured as a function of the momentum transfer, defined as $Q = (4\pi/\lambda) \sin\theta$, with λ being the neutron wavelength and 2θ the angle of scatter. Small angle scattering arises from differences in neutron coherent scattering length density (SLD) between nm to μm scale dispersed phases. Even for multimineralic rocks, it has been shown that the dominant SANS/USANS scattering contribution results from the embedded pore system and internal mineral-pore surfaces (two-phase approximation) (Anovitz et al., 2009; Radlinski, 2006) . In this case, the porosity is obtained from the scattering invariant, given by $Z = 2\pi^2\phi_1(1-\phi_1)(\rho_1^* - \rho_2^*)^2$,with ϕ_1 the porosity and ρ_1^* and ρ_2^* the SLD's of pore and mineral phase, respectively. For empty connected and unconnected pore spaces the SLD is zero. Application of fractal models has proven very useful for the description of the multiscale porosity with rough internal surfaces often found in rocks (Lo Celso et al., 2000; Triolo et al., 2000; Navarre-Sitchler and

Brantley, 2007). The determination of pore size distribution and internal surface area is performed using the PRINSAS software, which is based on the polydisperse hard sphere model (Hinde, 2004). SANS and USANS are uniquely suited to characterize the nanoscale porosity and internal surface area of rocks in a statistically meaningful way. Based on previous research (Anovitz et al., 2009; Jin et al., 2011), neutrons scatter in porous rocks from both pores and bumps on the pore-mineral interface. ,The linear dimension or spacing (Å) of these scatterers -- either pores or bumps -- equals 2.5/Q (Radlinski, 2006). Intensities of scattering at high Q ($1x10^{-3}$ < Q < 0.03 $Å^{-1}$) measured by SANS, correspond to scatterers of diameter or spacing *d*, 1 < *d* < 250 nm. USANS, measured at low Q ($3x10^{-5}$ < Q < $1x10^{-3}$ $Å^{-1}$), corresponds to scatterer dimensions or spacings of 250 nm < d < 8.3 μm.

Both SANS and USANS data were measured on DR-4, but only SANS data were collected successfully for DR-7. Due to high incoherent background at higher Q for both samples, SANS spectra were considered only for the Q range of 0.002 – 0.05 A^{-1} (5 < d < 250 nm). For the total porosity calculation we used combined SANS+USANS spectra for the Q range of $3x10^{-5}$ - 0.3 $Å^{-1}$ (0.8 nm - 8.3 μm).

Results

Drilling Observations

Drilled boreholes revealed repeated zones of highly fractured rock embedded within layers of disaggregated regolith material (Figure 4). In borehole B1W1, 2.1 m of overburden (road-building material and regolith) overlay the first zone of rock. From depths 2.1 m to 19 m, zones of rock and regolith alternate approximately every

2 m. Recovery of intact or fractured rock was only 8-60% for each 1.5 meter drilling run that passed through rock, indicating that 40-92% of the volume contained void space (fractures) or regolith (i.e., sample recovery percentages refer only to rock or hard saprock recovery; regolith, which was recovered as mud, is not included here). Recovery is given as 0% for zones shown as regolith in Figure 4, with the exception of the zone at 14.5-16.0 m depth where a total of 0.3 m of saprock (weathered rock) was recovered in several pieces. Between 19.0 and 33.5 m depth, neither rock nor saprock were recovered. At 33.5 m depth, another zone of rock was sampled before drilling was terminated at 37.2 m depth. Borehole B1W2 was drilled at slightly higher elevation than B1W1 on the road but aligned with the spine of a ridge. This second borehole passed through 4.1 m of disaggregated overburden (road fill or regolith) before the first zone of rock was reached. From 4.1 to 13.4 m, rock recovery was high (53-90% per 1.5 m drill run) and un-broken sections of core that were 0.3-, 0.46, 0.6-, and 0.9-m long were recovered in addition to numerous smaller pieces.

Throughout the drilling, recovery less than 100% indicated that some volume of the drilled section was occupied by open fractures and/or regolith. In drilling runs with low or zero recovery, wet mud was brought up by the coring apparatus – this material was interpreted as regolith that had been liquefied by the water flushed into the borehole to cool the drill bit.

Below 13.4 m depth in borehole B1W2 (Figure 4), recoverable rock was sparse, with zero recovery between 16.5 and 25.3 m, i.e., regolith. However, small intact saprock samples were recovered from between 13.1 and 14.8 m depth (11% recovery) and between 15.7 and 16.3 m depth (30% recovery including 0.2 m of rock fragments). At 25.3 m depth, another zone of rock was recovered before drilling was terminated at 27.0 m depth.

Rock samples recovered from both the borehole drilling on the road and on the exposed boulders are fine- to medium fine-grained, dark blueish or greenish grey (Figure 2). The rocks recovered from the deep drilling contained abundant natural fractures, many of which had weathering rinds that were up to 15 mm thick. Weathering rinds appeared as thin, reddish coatings along the exposed fracture.

Corestone measurements

The exposed corestones measured here and cored using the hand-held drill, were observed to have diameters of 0.5 – 3.0 m, although a few, partially buried corestones were > 3.0 m (Table 1). Therefore, the corestone size, calculated as the cube root of the measured volume, ranges from 0.5 – 2.6 m for the fully exposed corestones. As shown in Figure 2, corestones exposed at the land surface had very thin weathering rinds. These rinds were approximately 0.5 – 5.0 mm in thickness. The corestones themselves were greyish-blue in color whereas the rinds appeared whitish in thin section, terminating in reddish coloration toward the surface, similar to the rinds along fracture surfaces in the deep borehole samples. Un-weathered portions of the corestones were classified as fine-grained siltstone to coarse-grained sandstone. Corestones appeared relatively devoid of fractures. Sampled corestone size, elevation, and rind thicknesses are summarized in Table 1 with compositional data for selected samples shown in Tables 2-4.

Chemistry and mineralogy

Most of the rock samples collected (exposed corestones and deep borehole samples) can be chemically classified as basaltic-andesites based on the total alkali vs. silica content (TAS), although a few fall into the range of basalts or andesites (Table 2). Although visible grain size and color of un-weathered rocks vary slightly within the Bisley watershed, the bulk chemical composition is not highly variable with depth in the boreholes, between boreholes, or between boreholes and corestones (Figure 5; Table 2). Relative to the borehole rock samples, regolith recovered from the borehole cores had a higher CIA and contained less Ca, Na, Fe(II), and Mg and slightly more total Fe and Ti (Table 2). Exposed corestones that were sampled with a hammer appear more chemically variable than borehole samples, particularly in labile elements such as Ca, Mg, Na, and K, which is reflected in the variability in the CIA (Table 2, Figure 5A). Relative concentrations of elements that are commonly retained during weathering (Fe, Al, Si) are similar in corestone and borehole samples (Figure 5B).

Relative to the un-weathered rock, weathering rinds on the corestones are typically depleted in Ca, Mg, Na, and Si and enriched by more than 50% in Fe and hydrous components (LOI values) (Figure 6; Table 4). However, depletion of labile elements begins inboard of the core-rind boundaries in some instances (Figure 6). The CIAs of the rinds (~70) are higher than the CIAs of the cores (~60) and lower than the CIAs of the saprock samples recovered from the boreholes (~80). The CIAs of the hand-drilled cores (Table 4) are comparable to those of the subsurface corestones (Table 2). This data is in agreement with microscopic observations of Fe-rich material in the weathering rinds (Figures 7A-B).

Quantitative XRD analysis of visibly un-weathered rock samples from the B1W1 and B1W2 borehole cores revealed these rocks to be dominated by plagioclase and

chlorite with quartz, epidote, pyroxene, K-feldspar, tourmaline, and minor prehnite, biotite, calcite, illite, and kaolinite (Table 3). The concentrations of quartz and epidote vary to greater extent than other minerals although distinct variations with depth or between boreholes is not observed (Figures 8 and 5C, Table 3).

Thin section observations

Analysis of thin sections from corestones and borehole core samples by SEM revealed a complicated matrix that is spatially variable, with areas of microcrystalline quartz or microcrystalline albite forming a groundmass that surrounds large pyroxene crystals (Figures 9A-F). Less abundant microcrystalline K-feldspars are interspersed in the groundmass. Chlorite largely occurs as wispy strands interspersed with microcrystalline albite (Figure 9A). Accessory titanite (sphene), ilmenite, apatite, and pyrite have also been identified (Figures 9A, C, E).

Optical microscope images of the corestone thin sections revealed highly altered weathering rinds consisting of remnants of mineral grains (plagioclase and pyroxene) in an opaque matrix, presumably Fe(III)-oxides or -hydroxides (Figures 7A, B). Fe-rich regions were also observed under SEM. Alteration is also apparent in the visually non-weathered inner portions of the corestone samples, i.e., >10 mm from the outer rind edge. In particular, extensive porosity development can be seen in Fe(II)-rich minerals (amphibole, pyroxene, epidote) and to a lesser degree in plagioclase. Amphiboles, present as inclusions within larger pyroxene crystals, are extensively replaced with fine-grained chlorite (Figure 9B). SEM and optical images of corestones also revealed preferential porosity development along plagioclase

grain boundaries and within epidote grains (Figure 10). Accumulation of opaque, Fe-rich precipitate is observed within epidote pore space.

Neutron Scattering

Examples of neutron scattering data, taken on rind and core samples, are given in Fig. 11A. In both samples (DR-4 and DR-7), the rinds had higher scattering intensities than the cores. These higher intensities are indicative of higher porosity and/or specific surface area (SSA) – both of which can be calculated from neutron scattering data (Hinde, 2004) and both of which show an increase at the core-rind interface. The same Q range ($0.001 < Q < 0.05$ Å^{-1}) was used for both samples to determine nano-porosity (Table 5). The range in scatterer sizes that contribute to SANS for this Q range is referred to here as nanoporosity (in contrast to "total porosity" referred to below as inferred for SANS + USANS). For sample DR-4, SANS and USANS for both weathered (rind) and un-weathered (core) areas, a break in slope is observed on the log I – log Q plots at a scatterer dimension between 200 and 300 nm (Fig. 11A).

Some differences between samples were also observed. For example, DR-4 (from a corestone exhumed at a lower elevation) has higher porosity at large Q (small scatterers) than DR-7 (from a higher elevation) at every position. In addition, DR-7 exhibits smaller changes in porosity and SSA across the transects compared to DR-4. It is furthermore striking that, relative to the interior core, the porosity and SSA increases near the core-rind interface in DR-4 and then decreases in the outer rind while steady increases only are observed for DR-7 (Fig. 6 B,G).

Total porosity was also calculated by combining SANS and USANS data (scatterer dimensions in the range, 0.8 nm - 8.3 μm) for sample DR-4 (Table 5). Note that these methods are only capable of measuring scatterers smaller than ~10 μm , so "total" does not include porosity or SSA attributed to larger scatterers (e.g., pores > 10 μm). The total porosity of the protolith varies widely and is equal to 8.1 ± 4.1% (an average of the 3 core measurements). Porosity increases by a factor of ~2.5x across the core-rind interface but the decreases in the rind (Table 5). Therefore, the data are consistent with larger scatterers (probed by USANS) forming deeper in the core than smaller scatterers (probed by SANS). Interestingly, while SANS SSA did not change much at the core-rind interface, the combined SANS+USANS SSA (total SSA) exhibits a sharp increase at the interface. The SSA continues to grow and becomes more than 3x larger than the protolith SSA towards the rind edge (Fig. 6G).

Discussion

Chemical Weathering

A history of low- to moderate-grade metamorphism is reflected in the Bisley rocks by the presence of epidote, prehnite, pyrite, and tourmaline (Table 3, Figures 8-9). Additionally, microcrystalline quartz that is variable in abundance may reflect an episode of metasomatism in which Si-rich fluids permeated the volcaniclastic sediments non-uniformly (Figures 8 and 5C). Furthermore, all the Bisley rocks contain abundant Mg-rich chlorite, which is commonly associated with low- to medium-grade metamorphism and burial diagenesis. Therefore, replacement of amphibole by chlorite in otherwise un-weathered zones is likely the result of diagenetic or hydrothermal processes rather than weathering (Figure 9B).

In contrast to the metamorphism, weathering reactions are clearly observed in the ~mm's thick weathering rinds that surround corestones and fractures. The highly altered weathering rinds consist of remnants of grains of plagioclase and pyroxene in an opaque matrix of Fe(III)-oxides or –hydroxides and secondary clay minerals (Figures 7A, B). As expected, extensive porosity development can be seen in Fe(II)-rich minerals (amphibole, pyroxene, epidote) and to a lesser degree in plagioclase. However, inward from the core-rind boundaries, SEM and optical images also revealed preferential porosity development along plagioclase and pyroxene grain boundaries and within epidote, amphibole, pyroxene, and chlorite grains (Figures 7C, 9C, 10). Accumulation of opaque, Fe-rich precipitate is observed within epidote pore space. Thus, weathering fronts of these five minerals (plagioclase, pyroxene, epidote, amphibole, and chlorite) extend into the cores, inboard of the core-rind boundary. The core-rind boundary may coincide with the transition from advective (in the rind) to diffusive (in the core) transport of reactants (Ma et al., 2012; Sak et al., 2004; Sak et al., 2010).

Plagioclase and chlorite make up about 25 and 36 wt% (Table 3), respectively, of the visibly un-weathered corestones (exposed and subsurface) and these minerals are largely absent from the saprolite and significantly weathered in the weathering rinds. Hence the formation of disaggregated saprolite from rock is primarily attributed to chemical weathering reactions involving these two minerals. However, plagioclase or chlorite dissolution may not be the first chemical weathering reaction in the rock. Pyrite was also observed in thin sections taken from un-fractured sections of the deep drilled cores, but not in the sampled corestones or weathering rinds. Two possible explanations are that 1) pyrite is heterogeneously distributed in the bedrock or 2) pyrite weathering begins early and proceeds rapidly

such that no pyrite remains in the outer 20 cm of the corestones. The oxidation of Fe(II) primary minerals has been indicated as the incipient weathering reaction in the bedrock of other watersheds, including the quartz diorite of the neighboring Rio Icacos watershed (Buss et al., 2008) and the shale of the Susquehanna Shale Hills Critical Zone Observatory in central Pennsylvania (Brantley et al., Subm.). Thus oxidation of Fe(II) in pyrite or one of the other Fe(II)-containing primary minerals may be the initial weathering reaction. Alternatively, dissolution of minor calcite (Table 3) may also control initial porosity development as has been shown to be the case for granitoid rocks (White et al., 2005).

Fracturing and Corestone Development

Corestones exposed at the surface in the Bisley I watershed are generally angular to sub-rounded. We nonetheless interpret them as corestones that formed in the subsurface, starting as fracture-bounded bedrock blocks that were bathed in infiltrating meteoric fluids. With chemical weathering and fracturing, the blocks are inferred to have weathered in place, forming saprolite. However, we never observed rinds thicker than about 5 mm at land surface. Therefore, as rinds form, they must periodically slough or slake off. This mechanism is thus one way (or perhaps the predominant way) that saprolite forms. The progression of bedrock to weathering rind to saprolite is documented in the CIAs for the rock samples (~60), the corestone rinds (~70) and the borehole saprock (~80). With that model, we can explain the marked reduction of corestone size with elevation. In fact, no corestones are observed above ~380 masl and no corestones are exposed at the ridgetop, presumably because they have weathered away and only corestone-free saprolite

remains. Fletcher and Brantley (2010) modeled this process such that corestones diminished in size as plagioclase chemically weathered at the corestone surface.

However, it is apparent from the data present here that both chemical and mechanical weathering drives the disaggregation of the metavolcaniclastic rocks in the Bisley watershed. This weathering may occur at the grain or grain aggregate scale without rounding the corestones. Although occasional large exposed corestones are observed to have split along nearly vertical fractures after exposure, the angular forms of the corestones are not attributed to processes operative during surface exposure but rather to their angular shape throughout their lifetimes below and above ground. Indeed, oxidized weathering rinds were also observed along relatively angular fractures throughout the drilled rock cores (Figure 12). Apparently, corestone size diminution is occurring both by chemical weathering and disaggregation of the rind surface, and splitting along fractures in otherwise intact rocks. Almost all of this weathering and fracturing is occurring while the rock is in the subsurface. Similar coupling between physical fracturing and chemical weathering was observed in spheroidally weathering dolerites in South Africa, wherein Røyne et al. (2008) found that chemical weathering reactions drive both corestone size diminution and large-scale hierarchical fracturing by which corestones are broken apart internally.

The nature of the physical weathering is further indicated here by the rinds on corestone surfaces. No clear correlation between rind thickness and elevation is apparent in the data collected from either exposed corestones or drilled cores (Table 1, Figure13). From Figure 13, it follows that rinds exposed to weathering may normally detach when greater than about 6 mm in thickness. However, in landslide scarps near the ridgetops, small (approx. 5-20 cm), angular corestone remnants that

had weathered all the way through were also observed to be buried within the regolith. Thus it appears that with sufficient time in the subsurface, rind material could completely consume a small (10-30 cm) corestone.

The quartz diorite bedrock of the neighboring Rio Icacos watershed weathers spheroidally. The mechanism of this weathering has been attributed to reaction-driven fracturing whereby O_2 diffuses into low porosity bedrock and oxidizes Fe(II) within biotite, creating stress that leads to fracturing (Buss et al., 2008; Fletcher et al., 2006). The volcaniclastic bedrock of the Bisley watershed has significantly less biotite than the quartz diorite (0.9 and 9.5%, respectively, Table 3 and White et al., 1998), which may explain the lack of spheroidal weathering in the Bisley watershed. Instead, weathering rinds form and slough off via physical processes and weathering does not become limited by diffusion through the rinds. The lack of rounding of the corestones is consistent with sloughing off of the rind: other researchers have noticed that diffusion-limited weathering of basaltic-andesitic clasts causes rounding of the unaltered core (Ma et al., 2012). In contrast, in Bisley, the corestones remain relatively angular perhaps because the weathering rinds fall off.

Porosity and Surface Area

Increasing porosity and SSA during weathering has been observed with SANS and USANS for other weathering materials (Jin et al., 2011) and these changes are well known from other porosity and surface area measurements (Schulz and White, 1999; White and Brantley, 2003; White, 1990). The break in slope in plots of log I - log Q (Fig. 11A) has also been observed in weathered and un-weathered crystalline rocks (Bazilevskaya et al., this volume; Navarre-Sitchler et al., Subm.). The break in slope has been attributed to different types of scatterers in rocks: at

high Q, scattering occurs at bumps on pore-grain interfaces and at low Q, scattering occurs from pores that form within grains, on grain boundaries, and at triple grain junctions. In other words, the distribution of sizes of interfacial nanometer-sized bumps differs from the distribution of sizes of the larger pores. Given this interpretation, one explanation is that the break in slope (here, 200-300 nm) roughly corresponds to the smallest grain size or pore size in the rock. For example, no break in slope has been observed in weathered and un-weathered shales where the grain size is sub-micron (Jin et al., 2011).

Variations in porosity are attributed to the combined effects of dissolution and precipitation in the rinds. For both samples subjected to neutron scattering analysis, Ca and K depletion and Fe enrichment are documented by SEM-EDS (Fig. 6). Interestingly, these reactions occur deeper within the core in DR-4 than DR-7, i.e., that sample (DR-4) started to weather in the visually non-weathered portion of the corestone. Consistent with these data, porosity as measured with SANS and SANS+USANS starts to increase with respect to the protolith at ~3.5 mm, well below the visually observed core-rind interface in DR-4 (Fig. 6F-G). SEM images also document mineral alteration deep in the corestone (Figures 9-10). These results offer further evidence that weathering fronts do not necessarily coincide with weathering rinds such that weathering processes (porosity development and mineral alteration) may begin inboard of the visible rind.

Critical Zone Geometry

Two models for the geometry of the deep critical zone in the Bisley watersheds have been proposed previously (Fletcher and Brantley, 2010;

Schellekens et al., 2004). Schellekens et al. (2004) utilized geo-electric sounding to infer a subsurface structure that consists of 0.1-0.5 m of low-resistivity topsoil, 5-40 m of intermediate- to high-resistivity subsoil and saprolite; a deeper less-weathered, low-resistivity saprolite 20-25 m thick, and finally bedrock below depths of 20-60 m. Therefore, the depth of our boreholes, which terminated in rock at 27.0 and 37.2 m below the ground surface, are consistent with the depth to bedrock predicted by Schellekens et al. (2004). Although the resistivity data did not resolve the corestones embedded within the saprolite, it captured a general picture of the subsurface that is broadly consistent with our borehole data and the model of Fletcher and Brantley (2010). It should be noted that the depth to bedrock could be even greater than the depth of the boreholes as we cannot be certain that drilling terminated in bedrock and not in corestones. However, the borehole profiles, the resistivity profiles, and the models mentioned above all indicate that extensive weathering occurs at least 20 m below the stream channel; thus weathering depth is not controlled by the local stream level. In addition, highly oxidized saprolite and weathering rinds on the fracture surfaces of deep subsurface corestones reflect the presence of water and oxygen below the stream channel. Therefore, not all of the water in the watershed is discharged to the Bisley I stream. Presumably groundwater is transported via deep flowpaths and discharged to the larger tributary or Mameyes River at a lower elevation.

Fletcher and Brantley (2010) proposed that prior to the onset of the recent denudation regime, the ground surface and the bedrock weathering interface were parallel to each other and that the stream channel incised the saprolite (exposing corestones) until the relatively un-weathered bedrock was reached at low elevationBorehole drilling confirmed the presence of subsurface corestones within

the depth-range predicted by the Fletcher and Brantley model.Presumably, the corestones exposed at the surface are the remnants of the chemical weathering and fracturing that began in the subsurface. Many of the subsurface corestones are riddled with natural fractures, whereas exposed corestones tend to be massive. Consistent with this, although we only measured and sampled the largest of the aboveground corestones at any given locality (Table 1), many smaller corestones were observed at all locations and these stones are candidates to have split off from larger corestones along fracture surfaces.

Differences in the degree of fracturing were observed between the two boreholes. Zones of recoverable rock were larger and less fractured in borehole B1W2, which was drilled in alignment with a ridge, compared to borehole B1W1, which was drilled near the stream channel (Figure 4). In fact, roughly 30% of the material drilled at B1W2 was rock, while only 13% of the drilled material from B1W1 was rock. This could indicate that subsurface corestones are larger under the ridge than in the valley. Corestone size is a function of fracture spacing and duration and extent of weathering. Subsurface corestones at the same elevation in the two boreholes can reasonably be considered to have weathered for the same length of time and thus the difference in corestone size may indicate wider fracture spacing under the ridges – i.e., more resistant to weathering -- and narrower fracture spacing under the valleys. If weathering and erosion are faster where fracture spacing is closer and slower where fracture spacing is wider, as predicted by Fletcher and Brantley (2010) and if the two boreholes are representative of the subsurface, then it is furthermore possible that the valleys and ridges in the Bisley watersheds are controlled by the fracture spacing of the underlying bedrock.

Of course, other interpretations are also possible. For example, if more water flows through the subsurface under the valley than under the ridge, the additional water flux could enhance the extent of weathering and weathering could drive fracturing. Alternately, fracturing can be caused by geomporphic processes such that channel incision and removal of material causes enhanced fracturing in the valley bottom. Such differences in fracture distribution between valley floor and valley walls have been observed elsewhere (Wyrick and Brochers, 1981). Alternatively, some subsurface characteristics could be relict landslide material, particularly in local topographic low areas, such as borehole site B1W1.

The distribution of subsurface corestones is also important for understanding and predicting the distribution of nutrient pools. In our previous work on the spheroidally weathering corestones of the nearby Rio Icacos watershed, we found that the weathering flux of Fe(II) and P from primary minerals at the corestone-regolith interface was sufficient to support a thriving subsurface microbial community that was effectively isolated from the surface nutrient cycles by deep, highly leached regolith (Buss et al., 2005; Buss et al., 2010). Similarly, soil organic matter (SOM) content may be related to the location of subsurface corestones. Johnson et al. (2011) measured SOM in soil pits (10-60 cm deep) dug at 84 locations throughout the Bisley I watershed. Buried corestones limited effective soil depth to less than 60 cm in many of the pits, particularly in the valleys and on slopes. They found a stronger correlation between the concentration of SOM from each depth sampled (0-10 cm, 10-35 cm, 35-60 cm, and the combined 0-60 cm) and soil depth than to other variables such as the C:N ratio of local leaf litter. They attributed the relationship between SOM and soil depth to the greater stability (less erosion and disturbance) of the land surface where the soils are deeper (i.e., on the ridge tops). This

phenomenon is not exclusive to the tropics. In the Green Mountains of Vermont, USA, Johnson et al. (2009) also found a strong correlation between the concentration of SOM at 20+ cm and soil depth (20 cm to the C-horizon, the depth of which was not specified) and this was largely attributed to better draining of deeper soils. Soil depth in the Green Mountains was also limited by boulders (from glacial till) and the deeper soils were generally encountered at higher elevations, comparable to what has been observed in the Bisley watershed.

Conclusions

We presented a case study where drilling allowed investigation of weathering in the subsurface. We tested a model that was built upon the idea that weathering had left a thick packet of weathered material that graded upward from relatively un-fractured bedrock to corestones to saprolite to soil. Under this model, the Bisley I channel is incising through this regolith package, exposing saprolite and corestones at the land surface. Observations from this work that support the interpretation that exposed corestones are relicts of earlier weathering include the following: i) Every corestone analyzed had a weathering rind indicative of long-term exposure to corrosive fluids. ii) Drilling through the inferred zone of weathering encountered saprolite + corestones down to a depth of 37.2 m, equivalent to the inferred depth of transition from saprolite+corestones to relatively un-fractured bedrock. iii) CIAs document increasing degree of weathering such that subsurface and exposed corestones are the least weathered, followed by rinds on corestones, then saprock and finally, saprolite. Here, saprock refers to hand friable but intact weathered rock recovered by borehole drilling. In addition, we present geochemical evidence and neutron scattering data that are consistent with corestone diminution occurring via dissolution of primary minerals coupled to physical weathering processes, i.e.,

formation of secondary porosity and detachment of weathering rinds >6 mm in thickness. Finally, the angularity of each exposed corestone is consistent with weathering rind formation followed by detachment. Detachment precludes diffusion limitation during weathering which has been shown in other locations to cause rounding.

The sequence of weathering processes for these volcaniclastic rocks is inferred to be i) fracturing-induced exposure to meteoric fluids; ii) diffusion of reactants from the fluid into the protolith at the fracture interface; iii) dissolution of primary minerals (plagioclase, epidote, pyroxene, hornblende) and creation of porosity at or below the core-rind interface iv) precipitation of Fe oxides that decrease porosity in the outer part of the rind; and v) spalling of the altered surface leaving relatively fresh protolith to again weather. Given this sequence, the fact that DR-4 has higher nano-porosity (~5 < d <125 nm pores) as determined from SANS data (Fig. 3) is attributed to the fact that it has recently spalled to create a new surface rather than any differences in elevation or duration of weathering. The cycle of weathering and spalling has been observed in basaltic material in other regions (Hausrath et al., 2008). The lack of a porosity-elevation trend in the overall corestone data is likely symptomatic of the fact that the timescale of the weathering-spalling cycle is small compared to the overall duration of weathering of these corestones. Therefore the thickness and chemical nature of each rind is indicative only of the time since last spalling rather than the time since initiation of weathering of the entire corestone. A detailed analysis of the mineral weathering reactions in these rocks will be presented in a future paper.

Although geophysical techniques and surface observations provide a general picture of the geometry and weathering processes of the watershed, deep drilling

revealed the following important details that could not have been known otherwise: i) highly oxidized saprolite and fracture surfaces on corestones well below the elevation of the stream channel indicate that the stream is not the outlet for all of the water in the watershed; ii) the abundance of subsurface corestones and the degree of fracturing of the subsurface corestones differs between the borehole drilled in the valley and the borehole drilled under a ridge, suggesting that bedrock fracture spacing could play a role in the development of topography; iii) intensively fractured rock in the deep boreholes may indicate reaction-driven or other large-scale fracturing as a primary saprolite formation mechanism that is not evident in surface exposures. Therefore, although exposed corestones are interpreted here as relicts of subsurface weathering, they do not provide a complete picture of the processes occurring at depth. Finally, our results show that drilling is an invaluable tool for characterizing the deep critical zone as it provides insights into the hydrology, geomorphology, weathering, and nutrient cycles that impact the entire critical zone.

Acknowledgements

We acknowledge funding and support from the U.S. Geological Survey's Global Change Program, the National Research Program (NRP), and the Water Energy and Biogeochemical Budgets Program (WEBB) as well as from the NSF-Luquillo Critical Zone Observatory (NSF EAR-0722476). We acknowledge the support of the National Institute of Standards and Technology, U.S. Department of Commerce, in providing the neutron research facilities used in this work. Neutron scattering measurements utilized facilities supported in part by the National Science Foundation under Agreement No. DMR-0944772 and SLB acknowledges DOE

funding from OBES (DE-FG02-05ER15675) for the neutron scattering work. We also thank Peter Sak from Dickinson College for providing the hand-held drill; Andy Kurtz for helping us drill; the U.S. Forest Service for site access; and Carole Johnson, Pedro Diaz, Jesus Rodriguez, Sigfredo Torres-Gonzalez and Manuel Rosario-Torres from the U.S. Geological Survey. This manuscript was much improved by the editorial work of Stuart N. Lane and the comments of two anonymous reviewers and Sheila Murphy of the USGS. DRC was supported by the Center for Nanoscale Control of Geologic CO_2, an Energy Frontier Research Center funded by the U.S. Department of Energy, Office of Science, Office of Basic Energy Sciences. GR was sponsored by the Division of Chemical Sciences, Geosciences, and Biosciences, Office of Basic Energy Sciences (OBES), U.S. Department of Energy (DOE). Weare grateful to David Mildner for the help with USANS measurements.

References

Anderson SP, Dietrich WE. 2001. Chemical weathering and runoff chemistry in a steep headwater catchment. Hydrological Processes, **15**: 1791-1815.

Anderson SP, Dietrich WE, Brimhall GH. 2002. Weathering profiles, mass-balance analysis, and rates of solute loss: Linkages between weathering and erosion in a small, steep catchment. Geological Society of America Bulletin, **114**: 1143-1158.

Anovitz LM, Lynn GW, Cole DR, Rother G, Allard LF, Hamilton WA, Porcar L, Kim M. 2009. A new approach to quantification of metamorphism using ultra-small and small angle neutron scattering. Geochimica et Cosmochimica Acta, **73**: 7303-7324.

Bazilevskaya E, Lebedeva M, Pavich M, Rother G, Parkinson D, Cole D, Brantley S. this volume. Where fast weathering creates thin regolith and slow weathering creates thick regolith. Earth Surface Processes and Landforms: In Press.

Brantley SL, Buss H, Lebedeva M, Fletcher RC, Ma L. 2011. Investigating the complex interface where bedrock transforms to regolith. Applied Geochemistry, **26**: S12-S15.

Brantley SL, Holleran ME, Jin L. Subm. Probing chemical reactions underlying the Shale Hills Critical Zone Observatory, Pennsylvania (U.S.A.): Nested weathering reaction fronts. Submitted to Earth Surface Processes and Landforms.

Briggs RP, Cortes-Aguilar E. 1980. Geologic map of the Fajardo and Cayo Icacos quadrangles, Puerto Rico. U.S. Geological Survey.

Brimhall GH, Dietrich WE. 1987. Constitutive mass balance relations between chemical composition, volume, density, porosity, and strain in metasomatic hydrochemical systems: Results on weathering and pedogenesis. Geochim et Cosmochim. Acta, **51**: 567-587.

Bruijnzeel LA. 1991. Nutrient input-output budgets of tropical forest ecosystems: A review. Journal of Tropical Ecology, **7**: 1-24.

Buss HL, Bruns MA, Schultz MJ, Moore J, Mathur CF, Brantley SL. 2005. The coupling of biological iron cycling and mineral weathering during saprolite formation, Luquillo Mountains, Puerto Rico. Geobiology, **3**: 247-260.

Buss HL, Mathur R, White AF, Brantley SL. 2010. Phosphorus and iron cycling in deep saprolite, Luquillo Mountains, Puerto Rico. Chemical Geology, **269**: 52-61.

Buss HL, Sak PB, Webb SM, Brantley SL. 2008. Weathering of the Rio Blanco quartz diorite, Luquillo Mountains, Puerto Rico: Coupling oxidation, dissolution, and fracturing. Geochim. Cosmoch. Acta, **72**: 4488-4507.

Calmels D, Galy A, Hovius N, Bickle M, West AJ, Chen M-C, Chapman H. 2011. Contribution of deep groundwater to the weathering budget in a rapidly eroding mountain belt, Taiwan. Earth and Planetary Science Letters, **303**: 48-58.

Dietrich WE, Reiss R, Hsu M, Montgomery DR. 1995. A process-based model for colluvial soil depth and shallow landsliding using digital elevation data. Hydrological Processes, **9**: 383-400.

Dosseto A, Buss HL, Suresh PO. 2012. Rapid regolith formation over volcanic bedrock and implications for landscape evolution. Earth and Planetary Science Letters, **337-338**: 47-55.

Dosseto A, Turner SP, Chappell J. 2008. The evolution of weathering profiles through time: New insights from uranium-series isotopes. Earth and Planetary Science Letters, **274**: 359-371.

Eberl DD. 2003. User guide to RockJock - A program for determining quantitative mineralogy from X-ray diffraction data. U.S. Geological Survey Open File Report 03-78; 36 pp.

Eberl DD. 2008. User's guide to HandLens—A computer program that calculates the chemistry of minerals in mixtures. USGS Open-File Report 2008-1244; 37 pp.

Fletcher RC, Brantley SL. 2010. Reduction of bedrock blocks as corestones in the weathering profile: Observations and model. American Journal of Science, **310**: 131-164.

Fletcher RC, Buss HL, Brantley SL. 2006. A spheroidal weathering model coupling porewater chemistry to soil thicknesses during steady-state denudation. Earth and Planetary Science Letters, **244**: 444-457.

Frizano J, Johnson AH, Vann DR. 2002. Soil phosphorus fractionation during forest development on landslide scars in the Luquillo Mountains, Puerto Rico. Biotropica, **34**: 17-26.

Garcia-Martino AR, Warner GS, Scatena FN, Civco DL. 1996. Rainfall, runoff and elevation relationships in the Luquillo Mountains of Puerto Rico. Caribbean Journal of Science, **32**: 413-424.

Hausrath EM, Treiman AH, Vicenzi E, Bish DL, Blake D, Sarrazin P, Hoehler T, Midtkandal I, Steele A, Brantley SL. 2008. Short- and long-term olivine weathering in Svalbard: Implications for Mars. Astrobiology, **8**: 1079-1092.

Heartsill-Scalley T, Scatena FN, Estrada C, McDowell WH, Lugo AE. 2007. Disturbance and long-term patterns of rainfall and throughfall nutrient fluxes in a subtropical wet forest in Puerto Rico. Journal of Hydrology, **333**: 472-485.

Heartsill-Scalley T, Scatena FN, Lugo AE, Moya S, Estrada Ruiz CR. 2010. Changes in structure, composition, and nutrients during 15 yr of hurricane-induced succession in a subtropical wet forest in Puerto Rico. Biotropica, **42**: 455-463.

Heimsath AM, Dietrich WE, Nishiizumi K, Finkel RC. 1997. The soil production function and landscape equilibrium. Nature, **388**: 358-361.

Hinde AL. 2004. PRINSAS—a Windows-based computer program for the processing and interpretation of small-angle scattering data tailored to the analysis of sedimentary rocks. Journal of Applied Crystallography, **37**: 1020-1024.

Jin L, Rother G, Cole D, Mildner D, Duffy CJ, Brantley SL. 2011. Characterization of deep weathering and nanoporosity development in shale - A neutron study. American Mineralogist, **96**: 498-512.

Johnson KD, Scatena FN, Johnson AH, Pan Y. 2009. Controls on soil organic matter content within a northern hardwood forest. Geoderma, **148**: 346-356.

Johnson KD, Scatena FN, Silver WL. 2011. Atypical soil carbon distribution across a tropical steepland forest catena. CATENA, **87**: 391-397.

Jolly WT, Lidiak EG, Dickin AP, Wu T-W. 1998. Geochemical diversity of Mesozoic island arc tectonic blocks in eastern Puerto Rico. Geol. Soc. Am. Spec. Pap., **322**.

Kline SR. 2006. Reduction and Analysis of SANS and USANS Data using Igor Pro. Journal of Applied Crystallography, **39**: 895-9000.

Kurtz AC, Lugolobi F, Salvucci G. 2011. Germanium-silicon as a flowpath tracer: Application to the Rio Icacos watershed. Water Resources Research: In Press.

Lugolobi F, Kurtz AC, Derry LA. 2010. Germanium-silicon fractionation in a tropical, granitic weathering environment. Geochimica et Cosmochimica Acta, **74**: 1294-1308.

Ma L, Chabaux F, Pelt E, Granet M, Sak PB, Gaillardet J, Lebedeva M, Brantley SL. 2012. The effect of curvature on weathering rind formation: Evidence from Uranium-series isotopes in basaltic andesite weathering clasts in Guadeloupe. Geochimica et Cosmochimica Acta, **80**: 92-107.

Navarre-Sitchler AK, Cole D, Rother G, Jin L, Buss HL, Brantley SL. Subm. Porosity and surface area evolution during weathering of two igneous rocks. Geochimica et Cosmochimica Acta.

Navarre-Sitchler A & Brantley S. 2007. Basalt weathering across scales. Earth and Planetary Science Letters **261**: 321-334.

Nesbitt HW, Young GM. 1982. Early Proterozoic climates and plate motions inferred from major element chemistry of lutites. Nature, **199**: 715-717.

Ollier C, Pain C. 1996. Regolith, Soils and Landforms. Wiley: UK; 326 pp.

Pike AS, Scatena FN, Wohl E. 2010. Lithological and fluvial controls on the geomorphology of tropical montane stream channels in Puerto Rico. Earth Surface Processes and Landforms, **35**: 1402-1417.

Radlinski AP. 2006. Small-angle neutron scattering and the microstructure of rocks. In: Wenk HR (Editor), Neutron Scattering in the Earth Sciences. Reviews in Mineralogy and Geochemistry. Mineralogical Society of America: Chantilly, Virginia; pp. 363-397.

Riebe CS, Kirchner JW, Finkel RC. 2004. Erosional and climatic effects on long-term chemical weathering rates in granitic landscapes spanning diverse climate regimes. Earth and Planetary Science Letters, **224**: 547-562.

Roering JJ, Marshall J, Booth AM, Mort M, Jin Q. 2010. Evidence for biotic controls on topography and soil production. Earth and Planetary Science Letters, **298**: 183-190.

Røyne A, Jamtveit B, Mathiesen J, Malthe-Sørenssen A. 2008. Controls on rock weathering rates by reaction-induced hierarchical fracturing. Earth and Planetary Science Letters, **275**: 364-369.

Sak PB, Fisher DM, Gardner TW, Murphy K, Brantley SL. 2004. Rates of weathering rind formation on Costa Rican basalt. Geochimica Cosmochimica Acta, **68**: 1453-1472.

Sak PB, Navarre-Sitchler AK, Miller CE, Daniel CC, Gaillardet J, Buss HL, Lebedeva MI, Brantley SL. 2010. Controls on rind thickness on basaltic andesite clasts weathering in Guadeloupe. Chem. Geol.: In Press.

Scatena FN. 1989. An introduction to the physiography and history of the Bisley Experimental Watersheds in the Luquillo Mountains of Puerto Rico. USDA Forest Service: General Technical Report SO-72; pp. 22.

Scatena FN, Lugo AE. 1995. Geomorphology, disturbance, and the soil and vegetation of two subtropical wet steepland watersheds of Puerto Rico. Geomorphology, **13**: 199-213.

Schellekens JH, Scatena FN, Bruijnzeel LA, van Dijk AIJM, Groen MMA, van Hogezand RJP. 2004. Stormflow generation in a small rainforest catchment in the Luquillo Experimental Forest, Puerto Rico. Hydrol. Process., **18**: 505-530.

Schulz MS, White AF. 1999. Chemical weathering in a tropical watershed, Luquillo Mountains, Puerto Rico; III. Quartz dissolution rates. Geochimica et Cosmochimica Acta, **63**: 337-350.

Seiders VM. 1971. Geologic map of the El Yunque quadrangle, Puerto Rico. U.S. Geological Survey.

Silver WL, Scatena FN, Johnson AH, Siccama TG, Sanchez MJ. 1994. Nutrient availability in a montane wet tropical forest: Spatial patterns and methodological considerations. Plant and Soil, **164**: 129-145.

Smith AL, Schellekens JH, Diaz AM. 1998. Batholiths as markers of tectonic change in the northeastern Caribbean. Geol. Soc. Am. Spec. Pap., **322**: 99-122.

Tipper ET, Bickle MJ, Galy A, West AJ, Pomies C, Chapman HJ. 2006a. The short term climatic sensitivity of carbonate and silicate weathering fluxes: Insight

from seasonal variations in river chemistry. Geochimica et Cosmochimica Acta, **70**: 2737-2754.

Tipper ET, Galy A, Bickle MJ. 2006b. Riverine evidence for a fractionated reservoir of Ca and Mg on the continents: Implications for the oceanic Ca cycle. Earth and Planetary Science Letters, **247**: 267-279.

Triolo F, Triolo A, Agamalian M, Lin J-S, Heenan R, Lucido G, Triolo R. 2000, Fractal approach in petrology: combining ultra small angle, small angleand intermediate angle neutron scattering: Journal of Applied Crystallography, **33**: 863-866.

USDA NCRS. 2002. Soil Survey of Caribbean National Forest and Luquillo Experimental Forest, Commonwealth of Puerto Rico. USDA, Natural Resources Conservation Service: Washington D.C.; pp. 181.

West AJ, Galy A, Bickle M. 2005. Tectonic and climatic controls on silicate weathering. Earth and Planetary Science Letters, **235**: 211-228.

White AF. 2002. Determining mineral weathering rates based on solid and soute weathering gradients and velocities: application to biotite weathering in saprolites. Chemical Geology, **190**: 69-89.

White AF, Blum AE, Schulz MS, Vivit DV, Stonestrom DA, Larsen M, Murphy SF, Eberl D. 1998. Chemical weathering in a tropical watershed, Luquillo Mountains, Puerto Rico: I. Long-term versus short-term weathering fluxes. Geochimica et Cosmochimica Acta, **62**: 209-226.

White AF, Brantley SL. 2003. The effect of time on the experimental and natural weathering rates of silicate minerals. Chemical Geology, **202**: 479-506.

White AF, Peterson, M. L. 1990. Role of reactive surface area characterization in geochemical models. In: Melchior DL and Bassett RL (Editors), Chemical modeling of aqueous systems II. Am Chem Soc Symp Ser; pp. 461-475.

White AF, Schulz MS, Lowenstern JB, Vivit D, Bullen TD. 2005. The ubiquitous nature of accessory calcite in granitoid rocks: Implications for weathering and solute evolution, and petrogenesis. Geochimica et Cosmochimica Acta, **69**: 1455-1471.

Wyrick GG, Brochers JW. 1981. Hydrologic effects of stress-relief fracturing in an Appalachian valley. U.S. Geological Survey Water Supply Paper, **2177**: 51 pp.

Ziegler K, Chadwick OA, White A, Brzezinski MA. 2005. δ^{30}Si systematics in a granitic saprolite, Puerto Rico. Geology, **33**: 817-820.

Table 1. Physical Characteristics of Exposed Corestones

Sample	Elevation, (m)	Position	Dimensions (m)	Max. Size[1], (m)	Rind thickness, (mm ± stdev)	Notes
DR13	234	Stream channel	2.5 x 2 x 2	2.2	0	Fine-grained meta- siltstone; greenish color; pockmarked
DR12	235	Stream channel	2 x 2.5 x 2	2.2	0	Coarse-grained meta-sandstone; greenish color
DR11	247	Stream channel	3 x 0.5 x 1	1.1	1.1±0.1	Fine-grained meta- siltstone
DR10	248	Ridgetop	2 x 1 x 0.75	1.1	2.8±0.7	Coarse-grained meta- sandstone
DR2	263	Slope	> 3	>3	0	Coarse-grained meta- sandstone; dark color
DR1	281	Stream channel	> 3	> 3	0	Fine-grained meta- siltstone
DR3	312	Stream channel	3 x 3 x 2	2.6	1.6±0.3	Coarse-grained meta- sandstone
DR4	314	Edge of stream channel	1.5 x 1.5 x 1.5	1.5	3.3±0.3	Fine-grained meta- siltstone
DR5	319	Stream channel	1 x 0.5 x 0.5	0.6	9.2±2.2	Coarse-grained meta- sandstone
DR6	328	Stream channel	1.5 x 0.5 x 0.5	1.6	4.0±0.4	Fine-grained meta- siltstone
DR7	350	Slope	1.5 x 2 x 1.5	1.7	4.3±0.8	Fine-grained meta-siltstone
DR9	352	Slope	1 x 0.5 x 0.5	0.6	2.1±0.2	Fine-grained meta-siltstone
DR8	369	Stream channel	0.5 x 0.5 x 0.5	0.5	2.1±0.5	Coarse-grained meta-sandstone

[1] Corestone size calculated as the cubic root of corestone volume.

Table 2. Bulk Chemistry of Exposed and Subsurface Corestones

Depth (m)	Al_2O_3 (wt %)	CaO	Fe_2O_3 *total Fe*	FeO[1]	K_2O	MgO	MnO	Na_2O	P_2O_5	SiO_2	TiO_2	Ba (ppm)	Nb	Sr	Zn	Zr	CIA[2]
Exposed Corestones[3]																	
-	16.1	6.24	8.40	4.40	0.66	4.76	0.15	3.96	0.17	54.20	0.62	430	40	230	90	117	59.7
-	16.6	7.20	7.73	4.30	0.69	4.73	0.14	4.50	0.18	55.60	0.62	420	30	280	90	86	57.3
-	16.7	5.10	9.58	5.50	0.77	5.92	0.17	5.00	0.2	53.00	0.63	580	20	290	100	86	60.6
-	17.8	3.90	7.67	2.90	2.78	3.69	0.16	1.47	0.12	50.30	0.57	520	10	220	140	463	68.6
-	17.6	2.01	12.1	-	0.42	5.16	0.2	4.2	0.12	48.8	0.81	230	<10	150	129	100	72.6
-	17.8	5.37	8.88	-	0.78	4.8	0.2	4.7	0.08	50.7	0.66	720	10	280	60	70	62.1
-	18.8	6.15	8.70	-	0.60	4.45	0.2	2.9	0.12	48.9	0.65	940	10	310	97	70	66.1
-	17.5	7.08	8.84	-	0.51	4.84	0.2	4.1	0.14	50.5	0.65	270	<10	200	58	70	60.0
-	17.5	7.18	9.73	-	0.38	5.79	0.1	4.5	0.18	48.8	0.73	60	<10	150	110	120	59.2
-	17.8	13.9	6.49	-	1.28	1.98	0.1	2	0.14	52.7	0.5	110	<10	120	16	90	50.9
-	18.0	9.36	9.39	-	0.71	4.79	0.2	4.1	0.14	52	0.68	220	10	250	58	120	56.0
-	18.2	11.6	8.60	-	0.13	3.96	0.1	4.3	0.19	53.6	0.7	40	10	150	50	120	53.2
-	14.7	6.69	7.90	-	1.18	4	0.1	2.4	0.14	57.8	0.69	520	<10	450	62	110	58.9
-	15.6	4.18	8.49	-	1.25	3.68	0.1	2.3	0.24	55.4	0.75	560	<10	370	70	130	66.9
-	25.9	0.04	8.18	-	0.09	0.32	0.0	0	0.15	45.5	0.74	100	<10	<10	24	120	99.5
-	20.6	0.02	12.0	-	0.15	0.25	0.0	0	0.17	47.9	1.08	120	<10	<10	<5	180	99.2
Subsurface Corestones B1W1, Elevation 261 masl[4]																	
2.1	17.5	7.77	8.94	5.9	0.62	6.22	0.12	2.2	0.11	53.6	0.68	330	<10	640	79	90	62.3
3.4	15.9	8.19	7.83	6.2	0.53	4.31	0.55	4.3	0.14	53.4	0.65	340	<10	280	79	110	55.0
4.00	18.1	9.26	8.14	6.20	0.35	4.14	0.14	3.60	0.11	53.3	0.58	290	<10	290	76	70	57.8
11.0	16.2	5.62	7.90	6.00	1.88	4.13	0.09	1.50	0.14	59.3	0.60	820	<10	540	89	90	64.3
12.8	18.1	1.89	10.8	<0.1	1.61	3.55	0.16	0.40	0.10	47.5	0.96	1070	<10	160	135	130	82.3
15.5	20.3	1.16	9.92	<0.1	1.22	2.92	0.15	0.70	0.07	49.7	0.64	1000	<10	130	96	70	86.8
16.5	13.9	5.75	7.4	5.70	1.09	5.17	0.10	2.20	0.10	60.6	0.59	570	<10	440	65	80	60.6
16.7	16.9	7.20	9.9	7.50	1.30	7.59	0.14	2.70	0.11	50.9	0.73	570	<10	530	112	100	60.1

17.0	17.5	8.78	8.90	6.80	0.29	5.87	0.13	3.90	0.10	50.0	0.65	300	<10	350	80	60	57.4
17.4	16.9	9.16	8.62	7.00	0.18	5.58	0.13	4.10	0.08	49.8	0.61	80	<10	360	78	50	55.7
18.0	17.2	10.80	9.0	4.40	0.81	5.28	0.13	3.00	0.10	51.0	0.65	250	<10	410	76	50	54.1
36.0	17.9	7.24	9.16	7.40	1.51	5.88	0.14	2.20	0.11	50.4	0.73	800	<10	570	84	100	62.0
37.0	17.6	7.53	9.20	7.00	1.44	6.38	0.14	2.20	0.10	53.0	0.70	700	<10	590	79	80	61.2
Subsurface Corestones B1W2, Elevation 263 masl																	
4.4	16.7	7.58	9.13	6.30	0.62	5.79	0.12	2.10	0.11	52.1	0.66	290	<10	630	69	90	61.9
6.4	17.0	8.69	7.86	4.90	0.41	5.03	0.10	2.40	0.11	52.8	0.64	190	<10	630	68	90	59.6
8.4	16.9	7.38	7.85	5.90	0.53	4.52	0.10	2.60	0.10	52.9	0.62	240	<10	580	62	90	61.7
10.4	17.9	7.90	8.05	5.30	0.54	4.88	0.10	2.10	0.11	56.1	0.69	360	<10	900	68	100	62.9
12.0	16.8	6.80	8.15	6.10	0.58	5.22	0.11	2.30	0.10	54.0	0.62	360	<10	780	65	90	63.4
14.0	18.9	4.20	10.90	0.40	0.87	3.45	0.10	1.60	0.13	50.0	0.78	840	<10	500	86	90	73.9
15.8	16.5	8.00	9.8	5.90	0.89	6.64	0.14	3.10	0.20	51.7	0.67	510	<10	690	74	70	57.9
26.7	15.8	8.62	9.2	5.40	0.77	6.01	0.14	3.10	0.11	50.6	0.63	360	<10	540	74	70	55.9

[1]Ferrous Fe not determined for all samples.
[2]CIA = chemical index of alteration = $100(Al_2O_3)/(Al_2O_3+CaO+Na_2O+K_2O)$ (Nesbitt and Young, 1982).
[3]Exposed corestones in this table were sampled with a hammer (not a drill).
[4]Subsurface corestones in this table are rock samples, exclusive of weathered fractures, returned via wire-line during borehole drilling. Shaded rows indicate saprock samples recovered during drilling.

Table 3. Mineralogy of Exposed and Subsurface Corestones

Depth (m)	Quartz (wt. %)	K-spar	Plag	Oxides	Kaol	Chlorite	Amph	Pyx	Tourm	Calcite[1]	Epidote	Prehnite	Biotite/ Illite[2]
Exposed Corestones[3]													
-	6.9	6.2	46.6	0.0	0.0	24.5	2.2	10.5	-	-	-	-	3.2
-	25.4	7.9	22.3	0.5	6.6	21.3	1.9	3.0	2.9	-	1.0	4.2	1.9
-	21.6	5.6	31.3	0.3	0.3	23.0	0.4	6.1	2.4	-	0.5	5.3	1.2
-	1.0	3.2	38.6	0.0	0.8	16.3	1.9	11.5	0.9	-	20.2	0.5	2.1
-	11.2	9.5	10.8	0.0	0.8	2.0	1.8	11.6	3.8	-	35.1	4.5	2.6
-	0.9	1.5	42.2	0.0	1.4	26.2	1.2	9.9	0.0	-	11.9	0.0	1.5
-	5.9	2.5	41.0	0.1	1.3	26.4	0.3	6.9	0.9	-	0.1	10.6	2.0
-	9.5	2.4	30.4	0.0	5.2	20.3	0.6	5.4	2.6	-	1.6	15.5	4.5
-	4.3	3.5	43.9	0.1	1.7	30.3	1.7	8.0	0.0	-	2.4	0.7	1.2
-	5.3	1.9	39.5	0.0	2.4	28.8	0.0	3.8	0.0	-	0.4	16.3	0.3
Drilled Bedrock B1W1, Elevation 261 masl													
2.1	17.5	4.0	33.2	-	0.9	24.5	-	7.3	1.0	0.1	11.4	0.0	0.2
3.4	6.6	4.7	43.4	-	0.2	18.6	-	11.5	3.0	4.7	3.0	4.3	0.0
4.00	7.3	3.4	35.4	-	0.0	21.8	-	6.4	2.9	0.9	4.4	16.5	0.9
11.0	13.2	15.4	35.2	-	0.0	25.0	-	3.4	3.1	0.0	4.0	0.0	0.5
16.5	6.1	9.6	37.3	-	1.0	26.1	-	12.7	4.4	0.3	1.8	0.7	0.0
16.7	4.0	9.0	34.0	-	0.6	28.7	-	14.6	5.9	0.2	1.4	1.0	0.7
17.0	0.0	5.4	42.4	-	0.1	35.4	-	11.9	2.8	0.3	1.7	0.0	0.0
17.4	1.1	2.6	46.2	-	0.0	23.2	-	11.7	2.5	2.6	2.0	8.0	0.0
18.0	4.8	6.2	31.4	-	0.8	16.1	-	14.9	2.4	0.3	22.2	0.0	0.9
36.0	7.1	10.7	39.5	-	0.4	30.9	-	6.5	2.3	0.4	1.6	0.5	0.0
37.0	13.2	10.8	30.1	-	0.8	27.2	-	10.5	5.1	1.1	0.7	0.1	0.2
Drilled Bedrock B1W2, Elevation 263 masl													
4.4	15.2	3.8	31.4	-	0.3	25.0	-	7.5	5.4	0.2	10.6	0.0	0.6
6.4	14.6	2.5	30.1	-	0.1	20.4	-	8.5	3.7	0.6	18.5	0.0	0.9

8.4	15.9	1.3	41.3	-	0.0	19.9	-	5.8	3.0	1.3	9.6	1.2	0.9
10.4	19.4	2.7	32.9	-	0.0	22.2	-	4.6	4.7	0.1	11.8	0.2	1.4
12.0	18.2	3.3	34.1	-	0.7	22.9	-	4.4	4.1	0.1	10.7	0.0	1.4
15.8	6.8	4.5	36.0	-	0.8	18.9	-	13.3	3.3	0.3	10.6	0.0	5.6
26.7	5.9	3.6	35.9	-	1.2	18.9	-	14.2	4.7	0.3	13.1	0.0	2.1

[1]Dashed lines indicate that the mineral was not detected in the sample set.

[2]Biotite and illite were not definitively identified separately.

[3]Exposed corestones in this table were sampled with a hammer (not a drill).

Table 4. Chemical Changes Across Core-Rind Interfaces

Sample[1]	Elevation (m)	Al_2O_3 (wt %)	BaO	CaO	Fe_2O_3 *Total Fe*	K_2O	MgO	MnO	Na_2O	P_2O_5	SiO_2	SrO	TiO_2	LOI (900C)	Zr (ppm)	CIA[3]
dr-10 core	248	19.2	0.06	5.36	8.69	1.25	4.61	0.16	4.62	0.13	52.3	0.05	0.74	2.90	80	61.3
dr-10 rind		18.8	0.08	2.09	15.85	1.44	4.17	0.27	3.26	0.12	43.1	0.03	0.92	11.68	104	73.5
% difference[2]		-2.3	35.3	-61.0	82.4	15.3	-9.5	68.9	-29.3	-5.9	-17.6	-43.0	23.2	302.9	30.3	
dr-7 core	350	17.3	0.09	7.18	9.31	0.89	5.07	0.16	4.15	0.11	52.1	0.04	0.68	2.84	85	58.6
dr-7 rind		17.3	0.12	5.30	10.46	1.04	5.09	0.25	3.95	0.12	50.5	0.03	0.77	6.76	91	62.7
% difference		-0.1	38.0	-26.1	12.3	17.1	0.4	54.5	-4.7	3.6	-3.1	-16.1	12.2	138.0	7.3	
dr-8 core	369	17.7	0.26	7.61	8.95	1.08	5.24	0.15	4.05	0.10	50.4	0.03	0.64	2.78	70	58.1
dr-8 rind		19.5	0.31	2.89	13.76	1.21	3.76	0.13	2.77	0.12	42.2	0.02	0.77	11.71	85	73.9
% difference		10.7	18.7	-62.0	53.8	11.2	-28.2	-9.1	-31.7	12.3	-16.4	-30.5	21.2	320.7	21.1	

[1]Samples taken from corestones in Bisley stream channel using a hand-held paleomagnetic drill.

[2]Percent differences in concentration between cores and the corresponding weathering rinds were calculated as $(C_{rind}-C_{bulk})100/C_{bulk}$. Negative values indicate depletion in the rind relative to the core, while positive values indicate enrichment.

[3]CIA = chemical index of alteration = $100(Al_2O_3)/(Al_2O_3+CaO+Na_2O+K_2O)$ (Nesbitt and Young, 1982).

Table 5. Neutron Scattering Data

Distance[a] (mm)	Region	Density[b] (g cm^{-3})	SLD[c] (Å)	Porosity[d] (%)	Total[e] Porosity (%)	SSA[f] (m^2 g^{-1})	Total SSA (m^2 g^{-1})
Sample DR-7							
0.5	rind	3.10	4.05	1.16	na	0.89 ± 0.09	na
1.5	rind	3.10	4.05	1.14	na	0.65 ± 0.07	na
2.5	rind	3.10	4.05	1.09	na	0.63 ± 0.06	na
3.5	core	3.08	3.99	0.73	na	0.50 ± 0.05	na
4.5	core	3.08	3.99	0.78	na	0.55 ± 0.06	na
9.5	core	3.08	3.99	0.75	na	0.48 ± 0.05	na
Sample DR-4							
0.5	rind	3.16	4.14	2.65	13.8 ± 11.2	0.70 ± 0.07	4.57
1.5	rind	3.16	4.14	4.07	7.1 ± 2.0	0.91 ± 0.09	2.84
2.5	rind	3.16	4.14	5.12	22.4 ± 11.8	0.81 ± 0.07	1.65
3.5	core	3.08	4.14	2.48	7.6 ± 3.0	0.51 ± 0.06	1.36
4.5	core	3.08	4.01	1.67	12.4 ± 5.3	0.53 ± 0.05	1.44
9.5	core	3.08	4.01	1.86	4.2 ± 1.6	0.56 ± 0.06	na

[a] Average distance from the edge of the outer edge of the weathering rind.

[b] Mineral density determined from bulk chemical composition reported in Table 4.

[c] SLD = Scattering length difference

[d] Porosity determined from SANS = Small Angle Neutron Scattering (0.002 < Q < 0.05 Å^{-1}). [e] Total porosity of DR-4 was determined from the combined SANS + USANS (Q range: 1x10^{-3} < Q < 0.3 Å^{-1}). Error bars on total porosity indicate 95% confidence interval.

[f] SSA = Specific surface area determined from SANS. Total SSA = SSA determined from the combined SANS + USANS data.

Figure Captions

Figure 1. Map of volcaniclastic Bisley watersheds I and II. Quebradas I, II, and III are the Bisley streams. The two drilled boreholes are B1W1 and B1W2. *(Figure supplied in color for online publication).*

Figure 2. A. Simplified schematic view of a 100 m-thick weathering profile of *in situ* weathered bedrock blocks (corestones) underlying boulder-free saprolite, with the bedrock-corestone interface shown as horizontal. The first stage of critical zone development in the Bisley watershed is shown on the left, where corestones are shown schematically to decrease in size toward the land surface due to increased duration of weathering. The second stage of critical zone development is shown on the right, where corestones are exposed by a later episode of rapid erosion. **B.** Thick sections from corestones from different elevations in Bisley profile, Puerto-Rico. The outermost edge (top of the slides) shows the weathering rind development in cross-section. *(Figure supplied in color for online publication).*

Figure 3. A plot of the profile of the Bisley I stream channel (after Fletcher and Brantley, 2010). Below ~220 masl, the Bisley I joins with the Bisley II and III tributaries. The combined stream joins the Rio Mameyes along a bedrock-lined channel just above 50 masl. Fletcher and Brantley (2010) observed that the maximum size of corestones did not vary below 200 masl, but decreased with increasing elevation above 200 masl. Below 200 masl, the slope of the Bisley channel is invariant until joining with the river at 50 masl. The plane of the channel between 50 and 200 masl was interpreted to be the plane across which corestones emerge from the fractured bedrock, or the saprolite-bedrock interface. If the

weathering profile is roughly parallel to the bedrock-saprolite interface (as shown), the average weathering profile thickness is 135 m.

Figure 4. Diagram of boreholes drilled in the Bisley 1 watershed showing locations of recovered rock samples. Grey = fractured rock; white = granular material (i.e., saprolite or sediment). Regolith zones were mostly washed out during drilling without sampling although a few intact pieces of saprock were recovered. All rock recovered was highly fractured with fractures spaced at mms to cms. Dashed lines at bottom of the cores indicate the deepest extent of drilling into what is inferred here to be relatively un-weathered bedrock.

Figure 5. Ternary diagrams of Bisley rocks sampled from deep drilled boreholes or aboveground corestones. Data plotted here is for visibly un-weathered subsamples (weathered rinds were cut off before analysis). **A)** Borehole samples contain similar amounts of labile elements Ca, Mg, Na, and K, whereas corestone samples contain variable amounts of these elements indicative of weathering of some samples. **B)** Relative solid-state concentrations of total Fe, Al, and Si are similar in both borehole and corestone samples. **C)** High relative concentrations of quartz may be indicative of weathering in some of the corestone samples or evidence of hydrothermal alteration. *(Figure supplied in color for online publication).*

Figure 6. A-E) Data from corestone DR-7 (350 masl). **F-J)** Data from corestone DR-4. Vertical axis on all panels A-J is the distance from the outer edge of the weathered rind, in mm. **(A, F)** Photographs of thick sections with lines marking 1 mm spacing. **(B, G)** Changes in porosity and specific surface area (SSA) determined from neutron scattering data and normalized relative to the protolith (i.e., 9.5 mm). SSA (open triangles) determined from SANS data. Total SSA (closed triangles), measured only

on DR-4 (314 masl), was determined from SANS+USANS data. Note that these methods are only capable of measuring scatterers smaller than ~10 μm , so "total" does not include porosity or SSA attributed to larger scatterers (e.g., pores > 10 μm). **(C-E, H-J)** Tau values for major elements were calculated from EDS data using Al as an immobile element. Parent composition was chosen as an average of the compositions measured at ~6-8 mm from the rind edge, which were assumed to represent un-weathered rock based on visual observation *(Figure supplied in color for online publication).*

Figure 7. Optical microscope images (20X magnification) of corestone sample DR-3, which consists mostly of anhedral large grains of plagioclase, smaller pyroxene grains, and occasional biotite grains. **A)** Weathering rind – bulk rock interface, **B)** The weathering rind contains fine-grained opaque minerals; large, a highly weathered pyroxene grain and small, white irregular grains, which may be disintegrating plagioclase. **C)** The bulk rock (10 mm inward from the weathering rind) contains patches of a brown-greenish stain within plagioclase and pyroxene grains and inter-grain cracks. **D)** Biotite grain and chlorite-stained plagioclase in the bulk rock (15 mm from the edge). Abbreviations: Pl – plagioclase; Px – pyroxene, Bi – biotite. *(Figure supplied in color for online publication).*

Figure 8. Box and whisker diagram showing mineral contents of 18 visibly un-weathered core samples from boreholes B1W1 and B1W2 as determined by quantitative XRD (Eberl, 2003). Wide boxes indicate 25-75% of data and are divided by a line denoting 50%. Small boxes indicate the mean, whiskers extend to outliers, X symbols indicate 1-99% of the data and small horizontal lines indicate maximum and minimum values. Mineral names are abbreviated as follows: Plag = plagioclase,

Chl = chlorite, Qtz = quartz, Pyx = pyroxene, Epi = epidote, Kspar = K-feldspar, Tour = tourmaline, Prehn = prehnite, Biot = biotite, Cal = calcite, Kaol = kaolinite.

Figure 9. Backscattered SEM images of visibly un-weathered zones within a corestone rock sample from the Bisley 1 stream (A-C), a corestone exposed by a landslide (D), and core recovered from borehole B1W2 at ~8.4 m depth (E-F). **A)** Microcrystalline quartz (Qtz) and microcrystalline albite (Alb) are separated by a band of Fe, Mg chlorite (Chl). A biotite (Biot) crystal contains small inclusions of apatite. **B)** Amphibole (Amph) is visible embedded within clinopyroxene (Pyx), identified as augite. The interior of the amphibole crystals is altered to chlorite. **C)** Large pyroxene crystals are shown containing inclusions of titanite (sphene, Sph) and ilmenite (Ilm). **D)** Epidote (Epi) is distributed within microcrystalline quartz (Qtz). K-feldspar (KSpar) is also visible. **E)** Several zones of pyrite (Pyr) were found in this section of core. **F)** Crystals of calcic plagioclase (Plag) and pyroxene are shown surrounded by a groundmass of plagioclase, chlorite, titanite, and possibly other minerals. Images A-D were collected at the USGS in Menlo Park, CA. Images E-F were collected at the University of Bristol.

Figure 10. Secondary Electron SEM image of corestone sample DR-7 taken 23 mm from the rind edge showing preferential porosity development within an epidote grain.

Figure 11. A) Neutron scattering data, I versus Q, for the rind (2.5 mm from the outer edge of the rind) and core (9.5 mm from the outer edge of the rind) of corestone sample DR-4. The rind has a higher scattering intensity due to higher porosity. Q regions for SANS and USANS and corresponding scatterer diameter (pore size) are also shown. **B)** SANS spectra for corestone sample DR-7, with

distances in mm from the outer edge of the rind. The data from 9.5 mm represents the fresh rock. *(Figure supplied in color for online publication)*

Figure 12. A) Photograph of a section of rock core from borehole B1W2 ~5.5 m below the ground surface. A weathering rind is visible along a natural fracture. **B)** Close up image of the rind shown in A. *(Figure supplied in color for online publication).*

Figure 13. Rind thickness (mm) versus elevation (masl) for rock samples collected from exposed corestones and boreholes. Trends in rind thickness as a function of elevation are not apparent in either set of data, likely due to spalling off of thick rinds on exposed corestones at higher elevation. The R^2 is 0.12 for the borehole data, 0.42 for the corestone data (omitting the outlier), and 0.18 for the entire dataset (omitting the outliers).

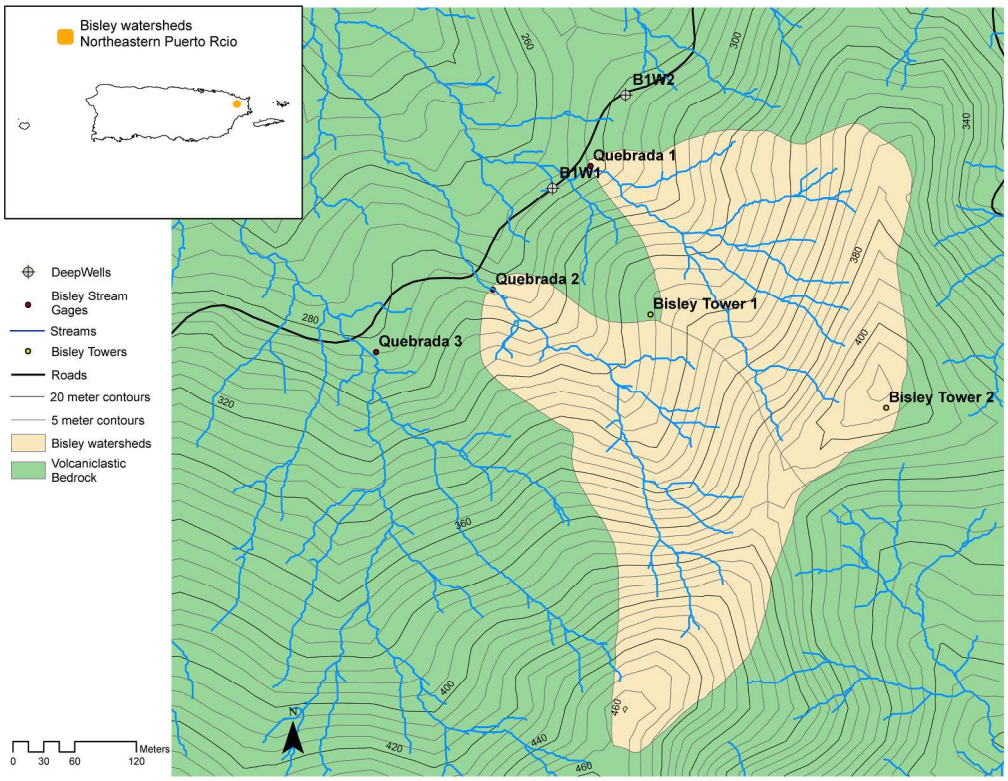

Figure 1. Map of volcaniclastic Bisley watersheds I and II. Quebradas I, II, and III are the Bisley streams. The two drilled boreholes are B1W1 and B1W2. (Figure supplied in color for online publication).
215x166mm (300 x 300 DPI)

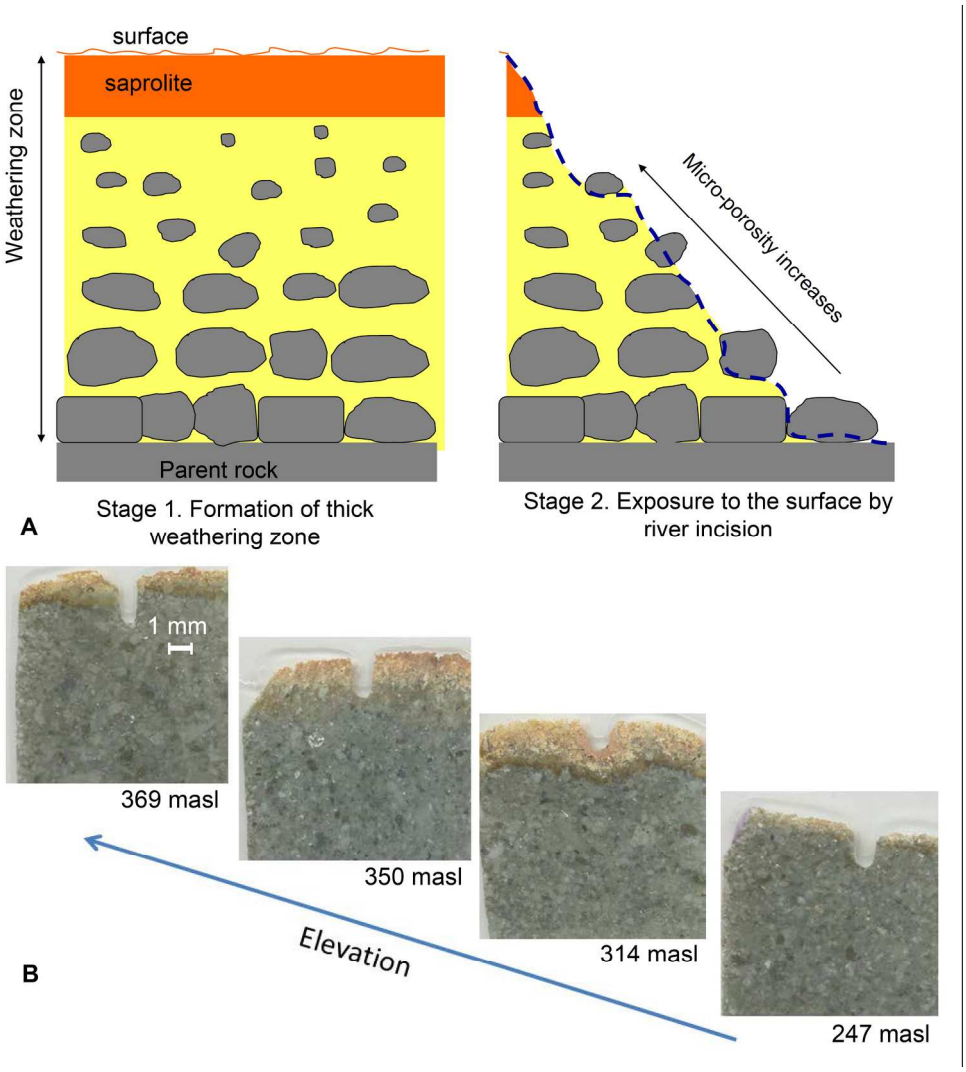

Figure 2. A. Simplified schematic view of a 100 m-thick weathering profile of in situ weathered bedrock blocks (corestones) underlying boulder-free saprolite, with the bedrock-corestone interface shown as horizontal. The first stage of critical zone development in the Bisley watershed is shown on the left, where corestones are shown schematically to decrease in size toward the land surface due to increased duration of weathering. The second stage of critical zone development is shown on the right, where corestones are exposed by a later episode of rapid erosion. B. Thick sections from corestones from different elevations in Bisley profile, Puerto-Rico. The outermost edge (top of the slides) shows the weathering rind development in cross-section. (Figure supplied in color for online publication).
201x213mm (300 x 300 DPI)

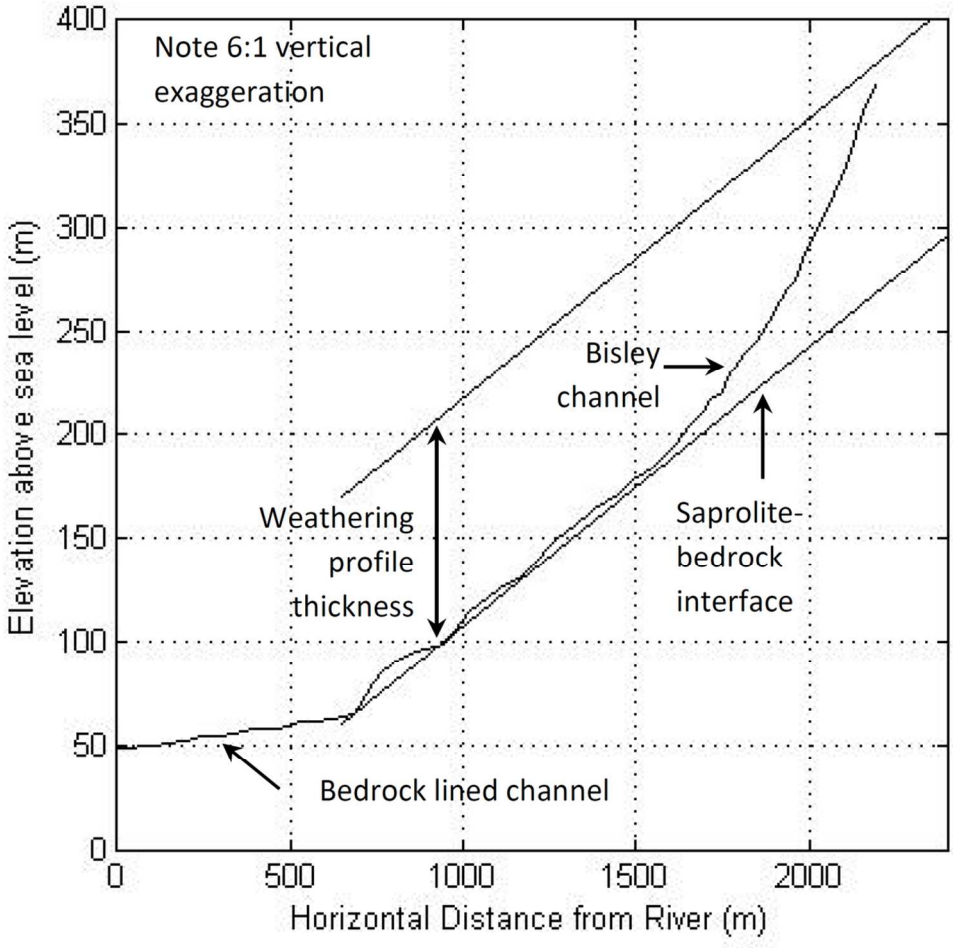

Figure 3. A plot of the profile of the Bisley I stream channel (after Fletcher and Brantley, 2010). Below ~220 masl, the Bisley I joins with the Bisley II and III tributaries. The combined stream joins the Rio Mameyes along a bedrock-lined channel just above 50 masl. Fletcher and Brantley (2010) observed that the maximum size of corestones did not vary below 200 masl, but decreased with increasing elevation above 200 masl. Below 200 masl, the slope of the Bisley channel is invariant until joining with the river at 50 masl. The plane of the channel between 50 and 200 masl was interpreted to be the plane across which corestones emerge from the fractured bedrock, or the saprolite-bedrock interface. If the weathering profile is roughly parallel to the bedrock-saprolite interface (as shown), the average weathering profile thickness is 135 m.
106x102mm (300 x 300 DPI)

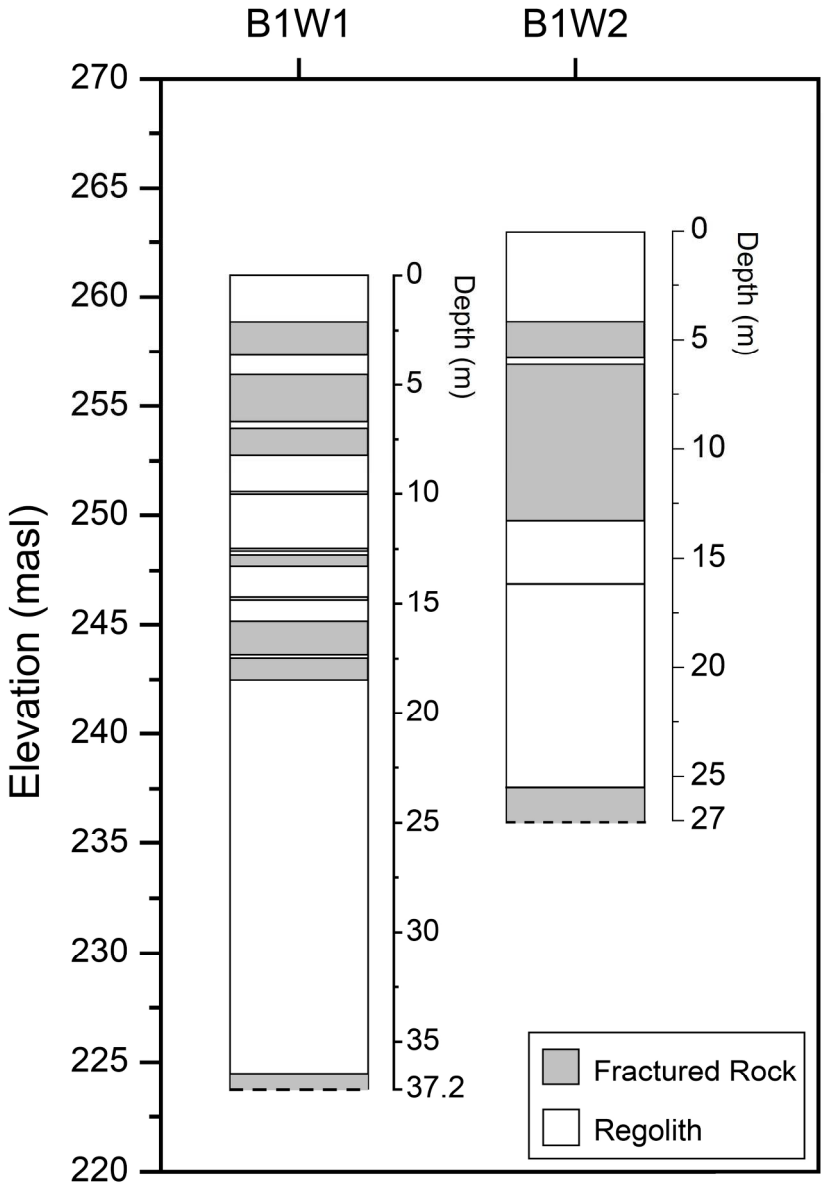

Figure 4. Diagram of boreholes drilled in the Bisley 1 watershed showing locations of recovered rock samples. Grey = fractured rock; white = granular material (i.e., saprolite or sediment). Regolith zones were mostly washed out during drilling without sampling although a few intact pieces of saprock were recovered. All rock recovered was highly fractured with fractures spaced at mms to cms. Dashed lines at bottom of the cores indicate the deepest extent of drilling into what is inferred here to be relatively un-weathered bedrock.
178x250mm (300 x 300 DPI)

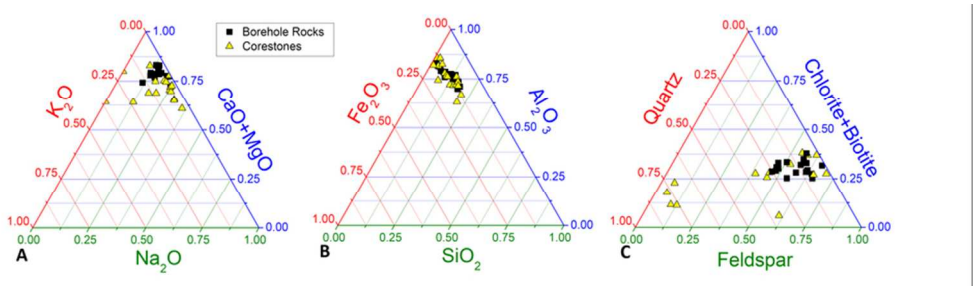

Figure 5. Ternary diagrams of Bisley rocks sampled from deep drilled boreholes or aboveground corestones. Data plotted here is for visibly un-weathered subsamples (weathered rinds were cut off before analysis). A) Borehole samples contain similar amounts of labile elements Ca, Mg, Na, and K, whereas corestone samples contain variable amounts of these elements indicative of weathering of some samples. B) Relative solid-state concentrations of total Fe, Al, and Si are similar in both borehole and corestone samples. C) High relative concentrations of quartz may be indicative of weathering in some of the corestone samples or evidence of hydrothermal alteration. (Figure supplied in color for online publication).
81x22mm (300 x 300 DPI)

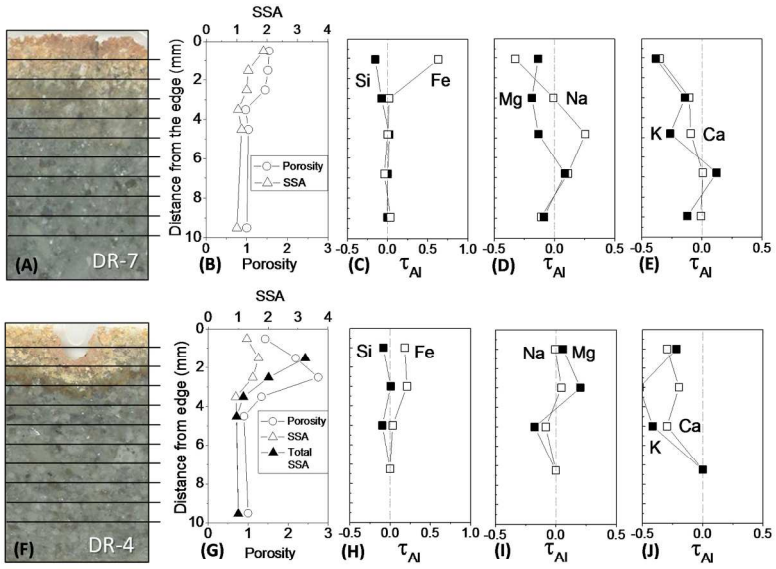

Figure 6. A-E) Data from corestone DR-7 (350 masl). F-J) Data from corestone DR-4. Vertical axis on all panels A-J is the distance from the outer edge of the weathered rind, in mm. (A, F) Photographs of thick sections with lines marking 1 mm spacing. (B, G) Changes in porosity and specific surface area (SSA) determined from neutron scattering data and normalized relative to the protolith (i.e., 9.5 mm). SSA (open triangles) determined from SANS data. Total SSA (closed triangles), measured only on DR-4 (314 masl), was determined from SANS+USANS data. Note that these methods are only capable of measuring scatterers smaller than ~10 μm , so "total" does not include porosity or SSA attributed to larger scatterers (e.g., pores > 10 μm). (C-E, H-J) Tau values for major elements were calculated from EDS data using Al as an immobile element. Parent composition was chosen as an average of the compositions measured at ~6-8 mm from the rind edge, which were assumed to represent un-weathered rock based on visual observation (Figure supplied in color for online publication).
209x148mm (300 x 300 DPI)

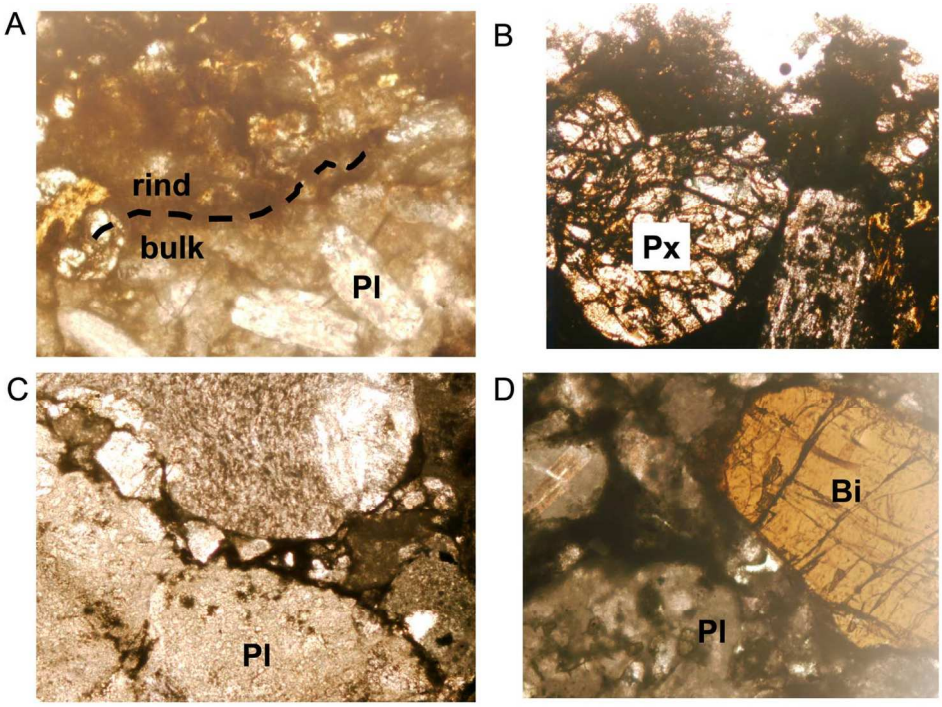

Figure 7. Optical microscope images (20X magnification) of corestone sample DR-3, which consists mostly of anhedral large grains of plagioclase, smaller pyroxene grains, and occasional biotite grains. A) Weathering rind – bulk rock interface, B) The weathering rind contains fine-grained opaque minerals; large, a highly weathered pyroxene grain and small, white irregular grains, which may be disintegrating plagioclase. C) The bulk rock (10 mm inward from the weathering rind) contains patches of a brown-greenish stain within plagioclase and pyroxene grains and inter-grain cracks. D) Biotite grain and chlorite-stained plagioclase in the bulk rock (15 mm from the edge). Abbreviations: Pl – plagioclase; Px – pyroxene, Bi – biotite. (Figure supplied in color for online publication).
209x148mm (300 x 300 DPI)

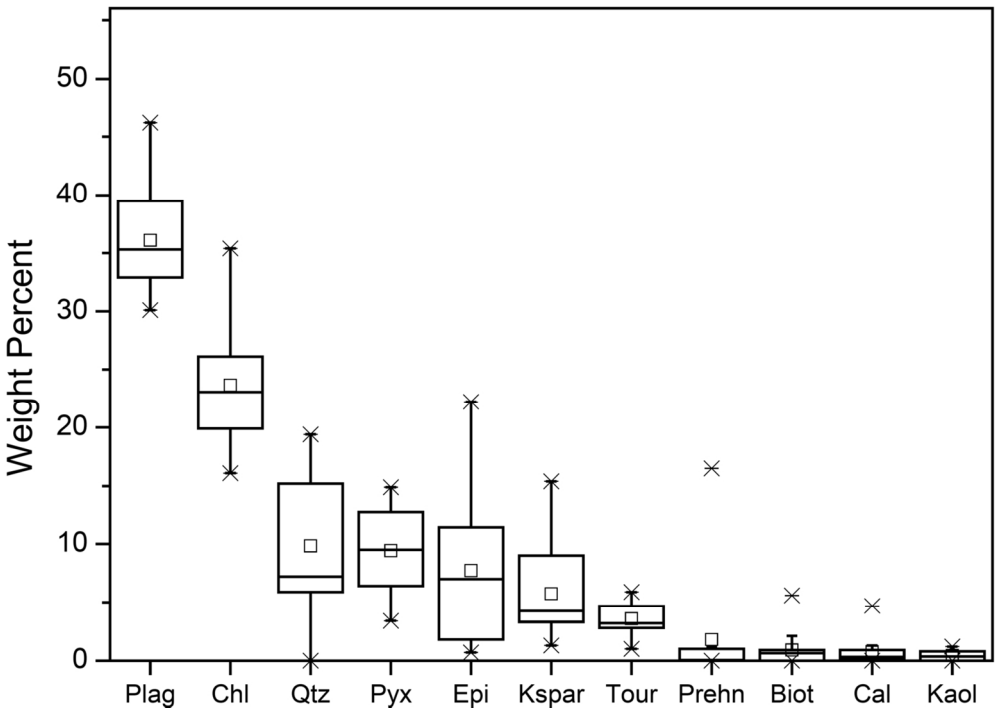

Figure 8. Box and whisker diagram showing mineral contents of 18 visibly un-weathered core samples from boreholes B1W1 and B1W2 as determined by quantitative XRD (Eberl, 2003). Wide boxes indicate 25-75% of data and are divided by a line denoting 50%. Small boxes indicate the mean, whiskers extend to outliers, X symbols indicate 1-99% of the data and small horizontal lines indicate maximum and minimum values. Mineral names are abbreviated as follows: Plag = plagioclase, Chl = chlorite, Qtz = quartz, Pyx = pyroxene, Epi = epidote, Kspar = K-feldspar, Tour = tourmaline, Prehn = prehnite, Biot = biotite, Cal = calcite, Kaol = kaolinite.
135x96mm (300 x 300 DPI)

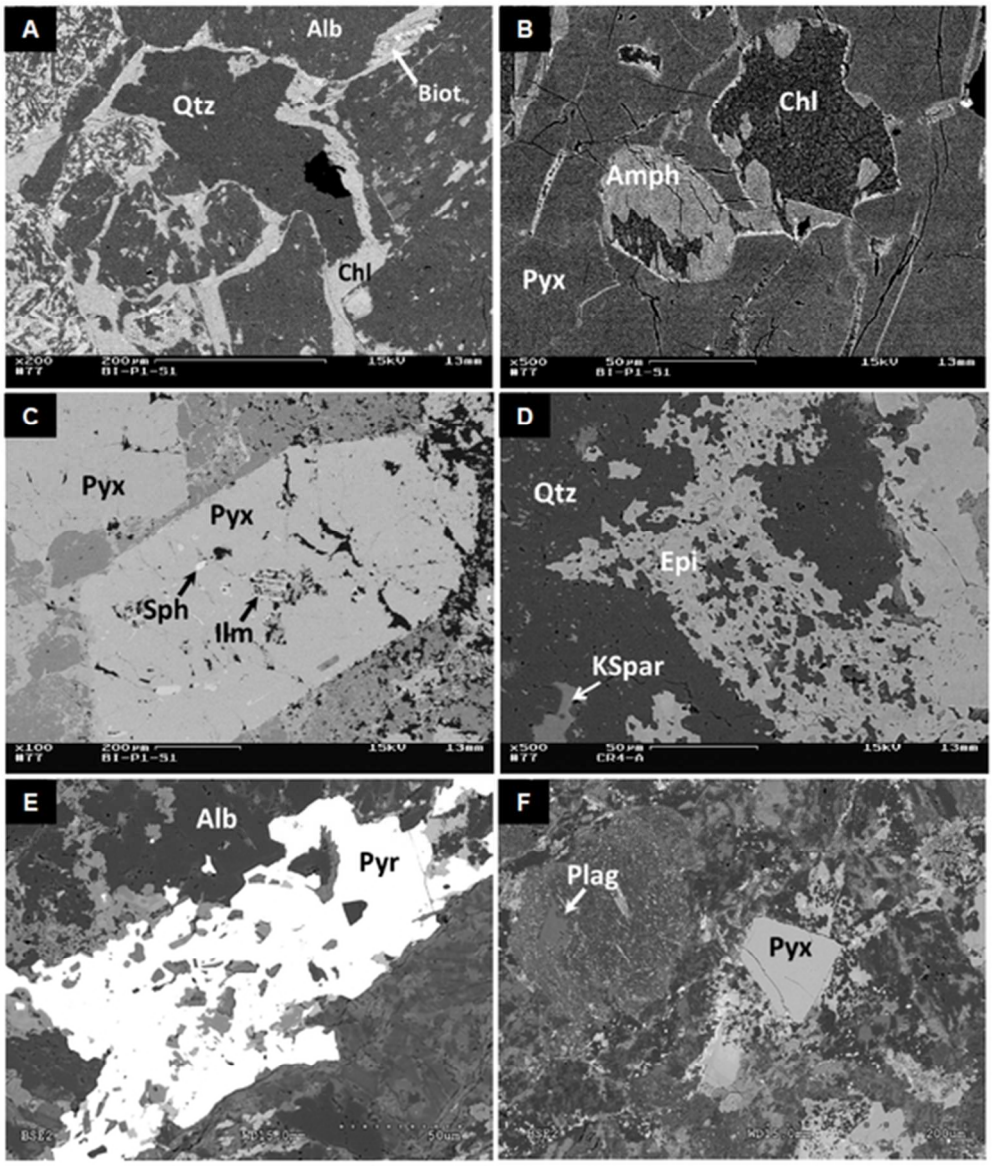

Figure 9. Backscattered SEM images of visibly un-weathered zones within a corestone rock sample from the Bisley 1 stream (A-C), a corestone exposed by a landslide (D), and core recovered from borehole B1W2 at ~8.4 m depth (E-F). A) Microcrystalline quartz (Qtz) and microcrystalline albite (Alb) are separated by a band of Fe, Mg chlorite (Chl). A biotite (Biot) crystal contains small inclusions of apatite. B) Amphibole (Amph) is visible embedded within clinopyroxene (Pyx), identified as augite. The interior of the amphibole crystals is altered to chlorite. C) Large pyroxene crystals are shown containing inclusions of titanite (sphene, Sph) and ilmenite (Ilm). D) Epidote (Epi) is distributed within microcrystalline quartz (Qtz). K-feldspar (KSpar) is also visible. E) Several zones of pyrite (Pyr) were found in this section of core. F) Crystals of calcic plagioclase (Plag) and pyroxene are shown surrounded by a groundmass of plagioclase, chlorite, titanite, and possibly other minerals. Images A-D were collected at the USGS in Menlo Park, CA. Images E-F were collected at the University of Bristol.
48x57mm (300 x 300 DPI)

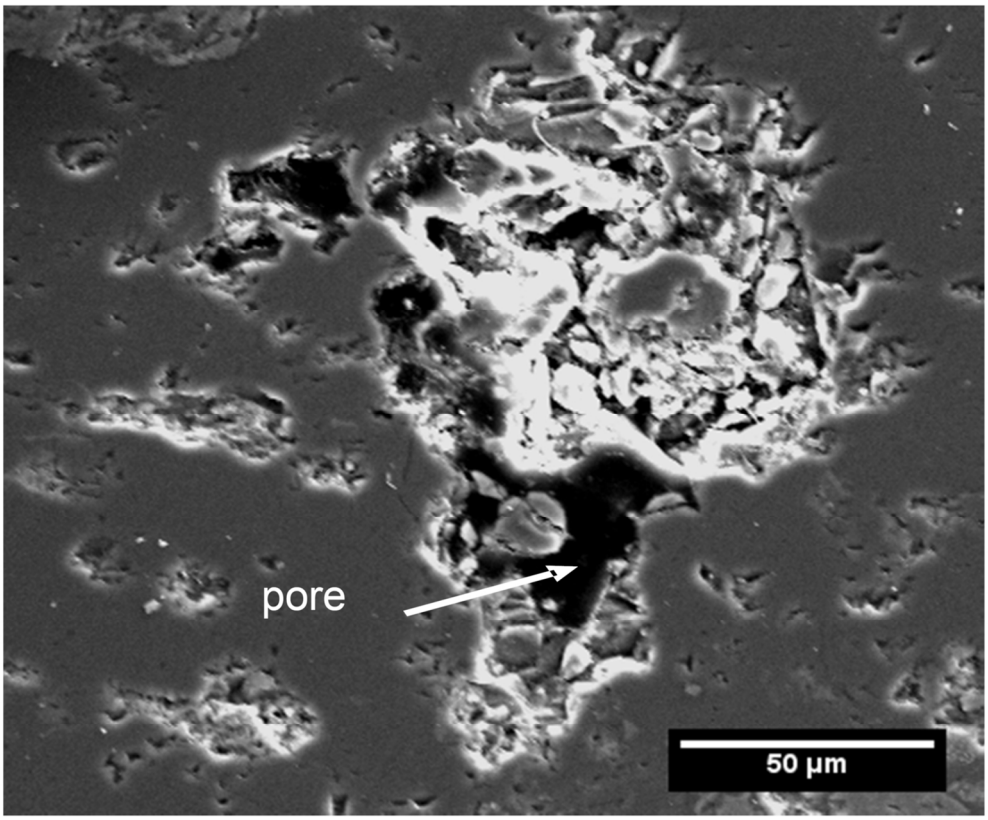

Figure 10. Secondary Electron SEM image of corestone sample DR-7 taken 23 mm from the rind edge showing preferential porosity development within an epidote grain.
123x101mm (300 x 300 DPI)

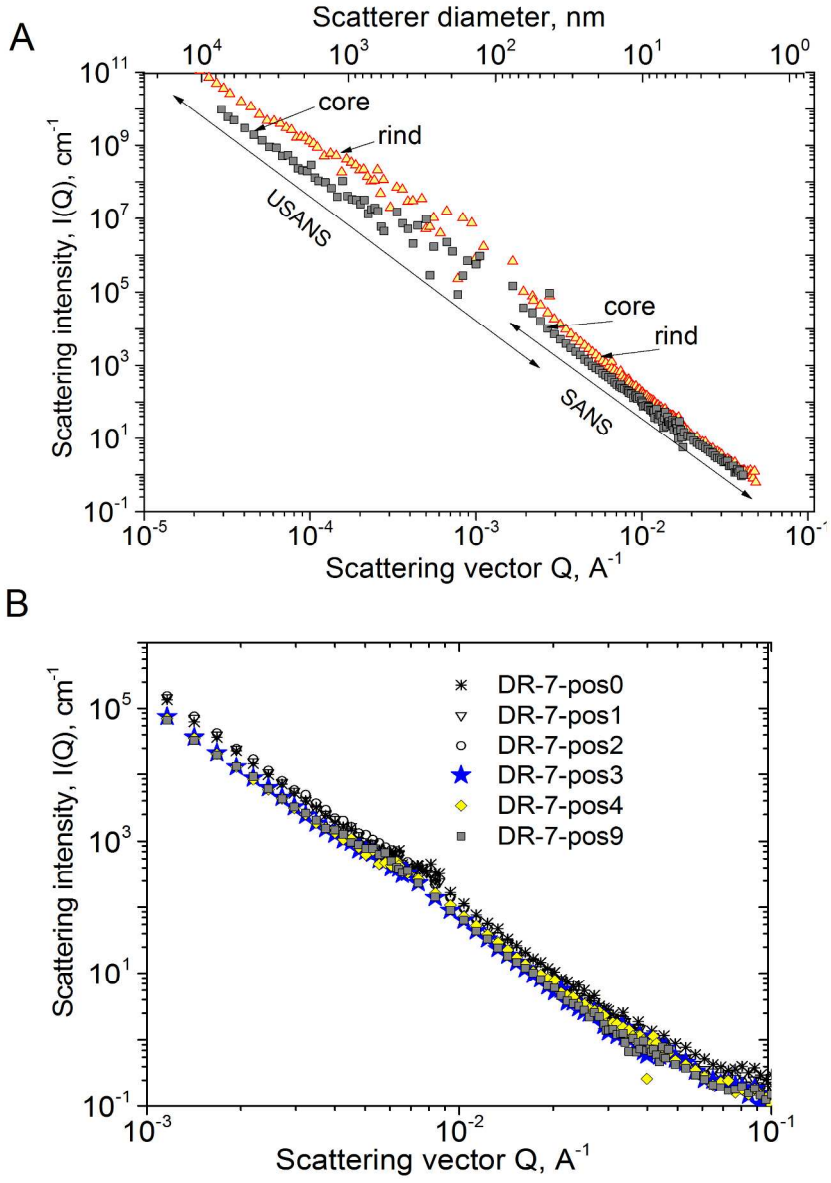

Figure 11. A) Neutron scattering data, I versus Q, for the rind (2.5 mm from the outer edge of the rind) and core (9.5 mm from the outer edge of the rind) of corestone sample DR-4. The rind has a higher scattering intensity due to higher porosity. Q regions for SANS and USANS and corresponding scatterer diameter (pore size) are also shown. B) SANS spectra for corestone sample DR-7, with distances in mm from the outer edge of the rind. The data from 9.5 mm represents the fresh rock. (Figure supplied in color for online publication)
205x271mm (300 x 300 DPI)

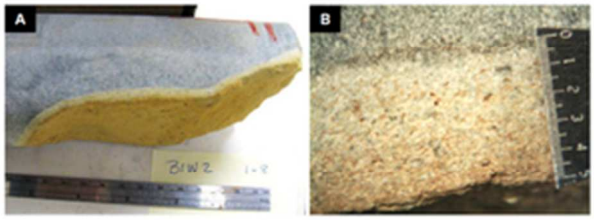

Figure 12. A) Photograph of a section of rock core from borehole B1W2 ~5.5 m below the ground surface. A weathering rind is visible along a natural fracture. B) Close up image of the rind shown in A. (Figure supplied in color for online publication).
25x15mm (300 x 300 DPI)

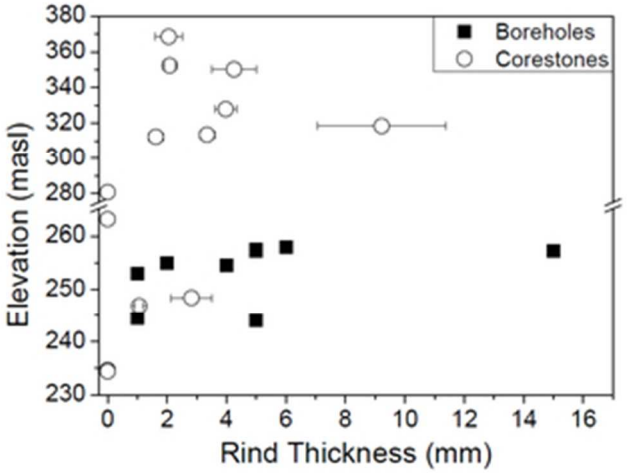

Figure 13. Rind thickness (mm) versus elevation (masl) for rock samples collected from exposed corestones and boreholes. Trends in rind thickness as a function of elevation are not apparent in either set of data, likely due to spalling off of thick rinds on exposed corestones at higher elevation. The R^2 is 0.12 for the borehole data, 0.42 for the corestone data (omitting the outlier), and 0.18 for the entire dataset (omitting the outliers).
26x20mm (300 x 300 DPI)